International Journal of Fatigue 164 (2022) 107109

Contents lists available at ScienceDirect

International Journal of Fatigue

journal homepage: www.elsevier.com/locate/ijfatigue

A Coarse-Mesh hybrid structural stress method for fatigue evaluation of Spot-Welded structures

Lunyu Zhang, Pingsha Dong *, Yuedong Wang [1], Jifa Mei [2]

Naval Architecture and Marine Engineering, University of Michigan, Ann Arbor, MI 48109, USA

ARTICLE INFO

Keywords:
Structural stress
Mesh-insensitive method
Hybrid method
Resistance spot welds
Fatigue evaluation

ABSTRACT

A hybrid structural stress method is presented for significantly simplifying spot weld representations in fatigue evaluation of complex spot-welded structures while retaining a high degree of accuracy in structural stress computation. The method is formulated by extracting nodal forces and moments around a group of domain elements connected to a spot weld represented by a regular beam element. Through a systematic decomposition technique, existing closed-form solutions, previously only valid for modeling single-spot weld test specimens, can now be used for calculating the relevant structural stresses under complex loading conditions in structures, as validated its ability in correlating fatigue test data.

1. Introduction

Typical automotive structures contain about 3,000 to 5,000 spot welds which serve as a cost-effective mean of joining metal sheets together in forming lightweight load-bearing structures, as recently discussed in the context of spot weld position optimization algorithms, e.g., by Bhatti et al. [1], Junqueira et al. [2], and Yan et al. [3]. As structural light-weighting becomes increasingly important due to new sustainability regulations, traditional quality definitions for spot welds connecting various high-strength lightweight sheet metals need to be revisited in light of the recent developments on quantitative quality acceptance criteria, e.g., those presented by Dong [4] and Zhang and Dong [5]. As the automotive industry increasingly relies on virtual prototyping, efforts for assuring structural durability place a major focus on spot welds which by design represent severe stress concentration sites, i.e., at interfacial notch around weld nugget edge. These sites are prone to fatigue damage under time-varying loads during service. Full vehicle or component level testing is time-consuming and cost-prohibitive in today's competitive environment. Therefore, reliable spot weld fatigue modeling methods capable of evaluating complex spot-welded structures become essential for achieving both structural reliability and cost-effectiveness in the development of advanced vehicle structures.

To achieve structural life predictability, any finite element (FE) based spot weld modeling methods must meet two basic requirements: (1) offering lab fatigue test data transferability among different lab specimen types, loading types, sheet thicknesses, etc.; (2) offering component life predictability by demonstrating that fatigue test data from simple lab specimens can be used to estimate fatigue life of a component. To meet the first requirement, it often needs to show that fatigue test data obtained from various forms of standard single spot-welded specimens, e.g., lap-shear (see Fig. 1a), coach-peel, and others [6,7,8,9,10,11] can be effectively correlated into a single narrow band. The second requirement can be affirmed through fatigue testing of selected structural components (e.g., modified H-shear component shown in Fig. 1b) to show that their fatigue lives can be reasonably estimated by using lab specimen test data (e.g., from simple lap-shear specimen shown in Fig. 1a).

As far as fatigue behaviors in single spot-welded lab test specimens are concerned, it has been shown that nominal stress (remote load divided by plate cross-section area) based S-N curves lack of data transferability, e.g., as shown in Rupp et al. [6], Radai and Zhang [7], and Salvini et al. [12], similar to the findings on fusion welded test specimens by Dong [13,14]. In contrast, a structural stress definition introduced by Radai and Zhang [7] was shown effective in correlating fatigue test data of lap-shear and coach-peel lab specimens. More recent investigations along this line can be found in [10,11]. With a mesh-insensitive structural stress method based on nodal forces and nodal

* Corresponding author.
E-mail address: dongp@umich.edu (P. Dong).
[1] Currently with Dalian Jiaotong University, China.
[2] Currently with American Axle Manufacturing, Detroit, MI.

https://doi.org/10.1016/j.ijfatigue.2022.107109
Received 14 March 2022; Received in revised form 18 May 2022; Accepted 27 June 2022
Available online 6 July 2022

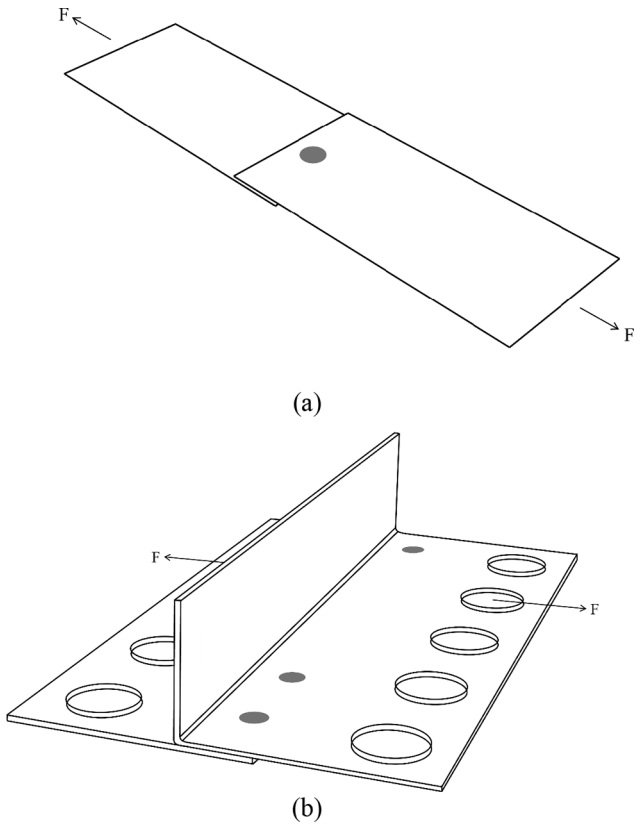

Fig. 1. Illustration of typical structural life modeling approach: (a) single spot-welded test coupons for generating laboratory fatigue test data and (b) complex spot-welded structure (e.g., one-half of a modified H-shear component) for validating structural life predictability based on lab coupon test data.

moments, Dong [14] and Kang et al. [15] further demonstrated the robustness of the structural stress based fatigue data correlation over a broad range of lab test specimen configurations. It should be noted there are also more recent developments in closed-form structural stress solutions for single spot-welded lab test specimens (Lin and Pan [9,16], Sung and Pan [17]) based on a rigorous plate theory by treating the spot weld as an embedded rigid inclusion. Once the structural stresses are computed with respect to spot welds, stress intensity factor solutions can be calculated in closed forms, e.g., those given by Radai and Zhang [7], Zhang [18], and more recently by Lin and Pan [9,16]. These recent developments offer a stress intensity factor range based fatigue data correlation that shows a similar effectiveness in consolidating fatigue test data (e.g., in [18]) to those when the mesh-insensitive structural stress range is used [13]. It should be mentioned that the relation between structural stress and stress intensity factor for spot welds under various types of loading conditions was initially established in Radai and Zhang [7] and more recently by Lin and Pan [9,16]. Therefore, for characterizing fatigue behaviors in spot-welded structures, the use of stress intensity factor is equivalent to the use of structural stress. Once a reliable structural stress method becomes available, either an equivalent structural stress range [13–15] or stress intensity factor range parameter expressed in terms of the structural stresses [18,19] can be used. In the latter case, an equivalent notch stress based on stress intensity factor solutions was shown effective in correlating simple lap-shear and couch-peel fatigue test data by Wei et al. [10].

Then, to fulfill the second requirement discussed above, a reliable method for determination of the structural stresses in complex spot-welded structures becomes essential for structural fatigue evaluation. Radai and Zhang [7], Zhang [18], Salvini et al. [12,20], and others developed various methods for computing structural stresses around spot welds using approximate analytical stress solutions by considering a plate with a rigid inclusion under simple loading conditions. Recently, Lin and Pan [9,16] and Sung and Pan [17] proposed closed-form structural stress solutions for a spot weld under various types of loading conditions including the self-balanced and the through-nugget loads on the lateral surface of the plate. Lin and Pan [9,16] emphasized that the self-balanced loads on the lateral surface of the plate should also be considered as well as the through-nugget forces and moments to obtain the full structural stresses around welds. However, it should be noted that all these solution methods, e.g., by Lin and Pan [9,16] and Sung and Pan [17], are only applicable for single spot-welded specimens commonly used in lab test environment, rather than multiple spot-welded complex components. The needs for addressing structural stress applications in complex structures were more clearly demonstrated most recently by Yang et al. [21] by performing fatigue test data correlations using components containing multiple spot welds. Their results show that existing forms of the structural stress method become less capable for correlating the test data as more spot welds are used in test specimens.

For applications in complex welded structures, it has been shown that the structural stress method proposed by Dong and his co-workers [14,15,22,23] offers a good mesh-insensitivity for modeling various complex structural specimens in fatigue evaluation, including spot-welded specimens [15]. In addition, the method has recently been extended to model multi-axial fatigue under both non-proportional loading conditions [24-26,32-34] in both time and frequency domains, as well as low-cycle fatigue [27-29,35]. However, the major limitation of the mesh-insensitive structural stress method (hereafter refers to a direct structural stress method or direct method in this paper) is that each spot weld needs to be explicitly represented with a ring of finite elements around the center of spot weld [15]. As a result, the direct method requires an extensive modeling effort, which can be impractical if dealing with a structure containing thousands of spot welds, e.g., in automotive structures.

To significantly simplify the modeling efforts while retaining the mesh-insensitivity observed in the direct method discussed above, this paper aims to develop a coarse-mesh hybrid method for fatigue evaluation of complex structures containing multiple spot welds under arbitrary loading conditions. The proposed coarse-mesh hybrid structural stress method is structured in three steps. In Step 1, an element domain is defined with respect to the shell finite elements directly connected to a spot weld represented by a beam element. Nodal forces and nodal moments can then be extracted from these domain elements. In Step 2, these nodal forces and moments are then decomposed into simple loading modes with respect to each spot weld involved, for which closed-form analytical solutions are already available, e.g., those given by Lin and Pan [9,16], and Sung and Pan [17]. In Step 3, the structural stresses calculated around a spot weld location corresponding to all decomposed simple loading modes are then superimposed to obtain the final structural stress solution. As such, there is no explicit representation of spot welds needed beyond the use of one beam element corresponding to each weld location, offering much-needed coarse-mesh modeling capabilities for structural applications. We then will show that the resulting hybrid structural stress procedure is robust and yields consistent structural stress results in comparison with the direct method. Finally, it can be shown that fatigue test data obtained from different types of spot-welded structures (single spot-welded and multiple spot-welded specimens) can be correlated into a single narrow band, demonstrating that the proposed coarse-mesh hybrid structural stress method offers both data transferability among single spot-welded lab specimens and components' life predictability of multiple spot-welded components.

2. Direct and Coarse-Mesh hybrid structural stress method

Before we present the new coarse-mesh hybrid structural stress formulation, the direct method is briefly summarized in the context of

modeling spot-welded structures, which will be used as a baseline or reference solution for comparing those obtained using the new coarse-mesh hybrid structural stress method which is the focus of the present study.

2.1. Direct structural stress method

The direct mesh-insensitive structural stress method proposed in Dong and his coworkers [14,15,22,23] has been shown to meet the above two requirements discussed in the previous section. For completeness, their method is briefly summarized here with a particular on its applications in modeling spot-welded structures.

Consider a close-up view around a spot weld of a multi-spot-welded H-shear component (taken from [8]), as shown in Fig. 2a. Fig. 2b shows a through-thickness (t) cross-section cut plane containing the spot weld and the typical local stress distributions at the weld nugget edge, e.g., within the bottom sheet. The corresponding statically equivalent structural stress definition in terms of through-thickness membrane σ_m and bending σ_b is given in Fig. 2c. As shown in Fig. 2b, the normal stress $\sigma_x(z)$ and the transverse shear stress $\tau(z)$ represent local through-thickness distributions caused by the corresponding remote forces (P1-P3) and moments (M1-M3), which are typically highly nonlinear, as a result of the sharp notch tip at the nugget edge.

As presented in Dong [13], the normal structural stress consists of two parts:

$$\sigma_s = \sigma_m + \sigma_b \tag{1}$$

where σ_m and σ_b are the membrane stress component and the bending stress component, respectively. Similarly, the local transverse shear stress $\tau(z)$ effects can be captured by the corresponding statically equivalent transverse shear structural shear stress, which has been shown not significant in typical structural applications [14] and will not be considered further in this study.

To extract the membrane and bending structural stress components in Eq. (1) by the means of the direct method, a spot weld needs to be explicitly modeled, as illustrated in Fig. 3. As such, as shown in Fig. 3a, the weld nugget area is typically represented by either shell elements or rigid beam elements with multiple point constraints (MPCs). In addition, a ring of shell elements is used for extracting nodal forces and moments along the inner ring edge (i.e., weld nugget notch edge) that are computed from a typical finite element analysis. These nodal forces and moments in the global coordinate system at nodal positions N_1 through N_i (see Fig. 3b) are then transformed into nodal forces and moments with respect to the local coordinate system (r, θ, and z), defined with respect to weld nugget center.

Based on the work equivalent argument that the work done by the nodal forces/moments is equal to the work done by the distributed line forces/moments, the rotated nodal forces and moments are then converted to the line forces and moments around the nugget edge line. This is done through a system of simultaneous equations given by Dong [14] and Dong et al. [22], e.g., for converting nodal forces to nodal line forces along the weld nugget edge line (also referred to weld line), as:

$$\begin{Bmatrix} F_1 \\ F_2 \\ F_3 \\ \cdot \\ \cdot \\ F_{n-1} \end{Bmatrix} = \begin{bmatrix} \frac{(l_1+l_{n-1})}{3} & \frac{l_1}{6} & 0 & 0 & .. & \frac{l_{n-1}}{6} \\ \frac{l_1}{6} & \frac{(l_1+l_2)}{3} & \frac{l_2}{6} & 0 & .. & .. \\ 0 & \frac{l_2}{6} & \frac{(l_2+l_3)}{3} & \frac{l_3}{6} & .. & .. \\ .. & .. & .. & .. & .. & .. \\ .. & .. & .. & .. & .. & .. \\ \frac{l_{n-1}}{6} & 0 & 0 & 0 & \frac{l_{n-2}}{6} & \frac{(l_{n-2}+l_{n-1})}{3} \end{bmatrix} \begin{Bmatrix} f_1 \\ f_2 \\ f_3 \\ \cdot \\ \cdot \\ f_{n-1} \end{Bmatrix} \tag{2}$$

where $f_1, f_2, f_3, \ldots, f_{n-1}$ are the local line forces at nodal points 1, 2, 3, …, $n-1$ and $F_1, F_2, F_3, \ldots, F_{n-1}$ are local nodal forces in local coordinate systems at the nodal points 1, 2, 3, …, $n-1$. since the weldline along the nugget periphery is closed, the local line force at nodal point n is the same as the local line force at nodal point 1. Similarly, the local line moments can be calculated using the local nodal moments using the same simultaneous equations, Eq. (2). With the calculated local line forces and line moments, structural stress is then calculated at each nodal point on the periphery of the nugget. The structural membrane stress component σ_m and bending stress component σ_b at each nodal point are calculated as:

$$\sigma_m = \frac{f_R}{t} \tag{3}$$

$$\sigma_b = \frac{6m_\theta}{t^2} \tag{4}$$

where t is plate thickness, f_R is local line force in the local r direction, and

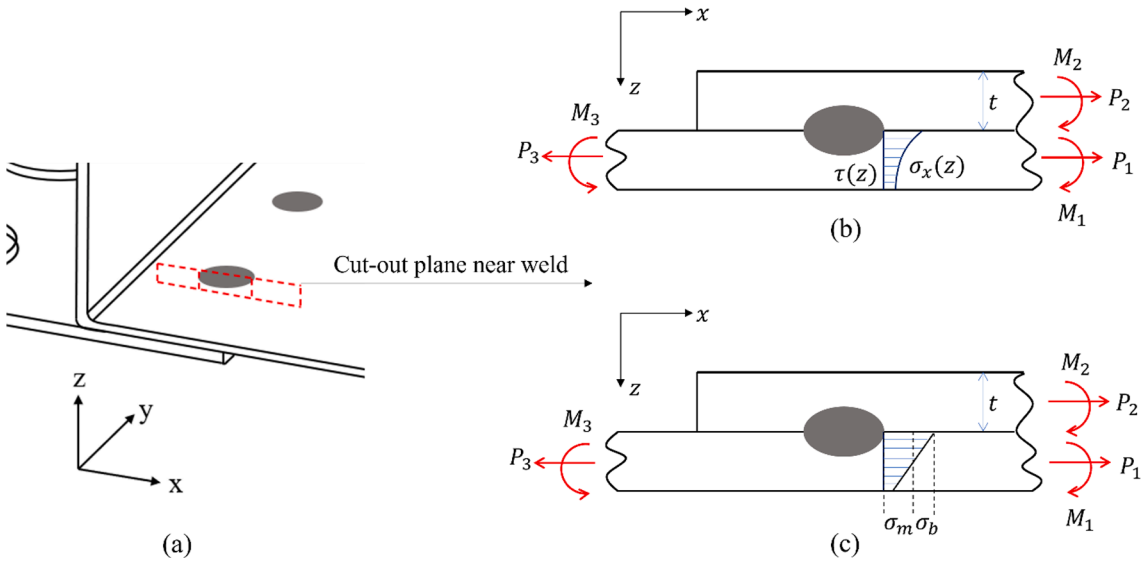

Fig. 2. (a) Close-up view around a spot-weld in the modified H-shear component, (b) through-thickness cut plane view of a spot weld and illustration of local stress distributions at weld nugget edge; and (c) statically equivalent structural stress definition.

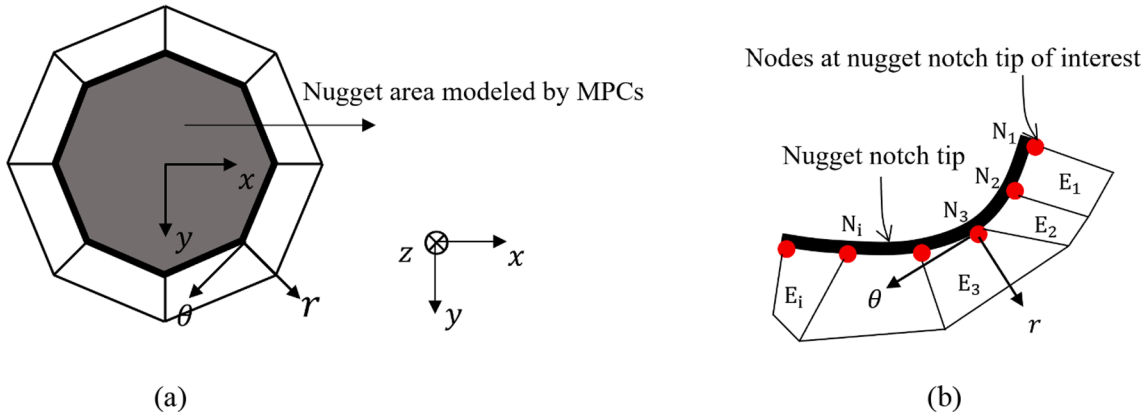

Fig. 3. (a) Explicit spot weld representation and local coordinated system at a spot weld and (b) the close-up view of the nodes around weld nugget edge.

m_θ is local line moment about the local θ axis.

To demonstrate the mesh-insensitivity of the structural stress calculated according to Eqs. (2)–(4), Fig. 4 shows a lap-shear specimen modeled by two shell element models (see Fig. 4a) with different element sizes around the weld nugget and a 3D solid element model (Fig. 4b) as presented in Dong et al. [22]. The resulting structural stress based stress concentration factor (SCF) results (normalized by remote nominal stress) are shown in Fig. 5. The mesh-insensitivity of the SCF results around the weld nugget edge is evident. Further details and examples can be found in Dong et al. [22] and Kang et al. [15], including demonstrations of S-N data transferability.

However, as discussed above and shown in Fig. 3, the direct structural stress method requires explicit modeling of spot welds and imposing constraints (i.e., MPCs) between top and bottom sheets around

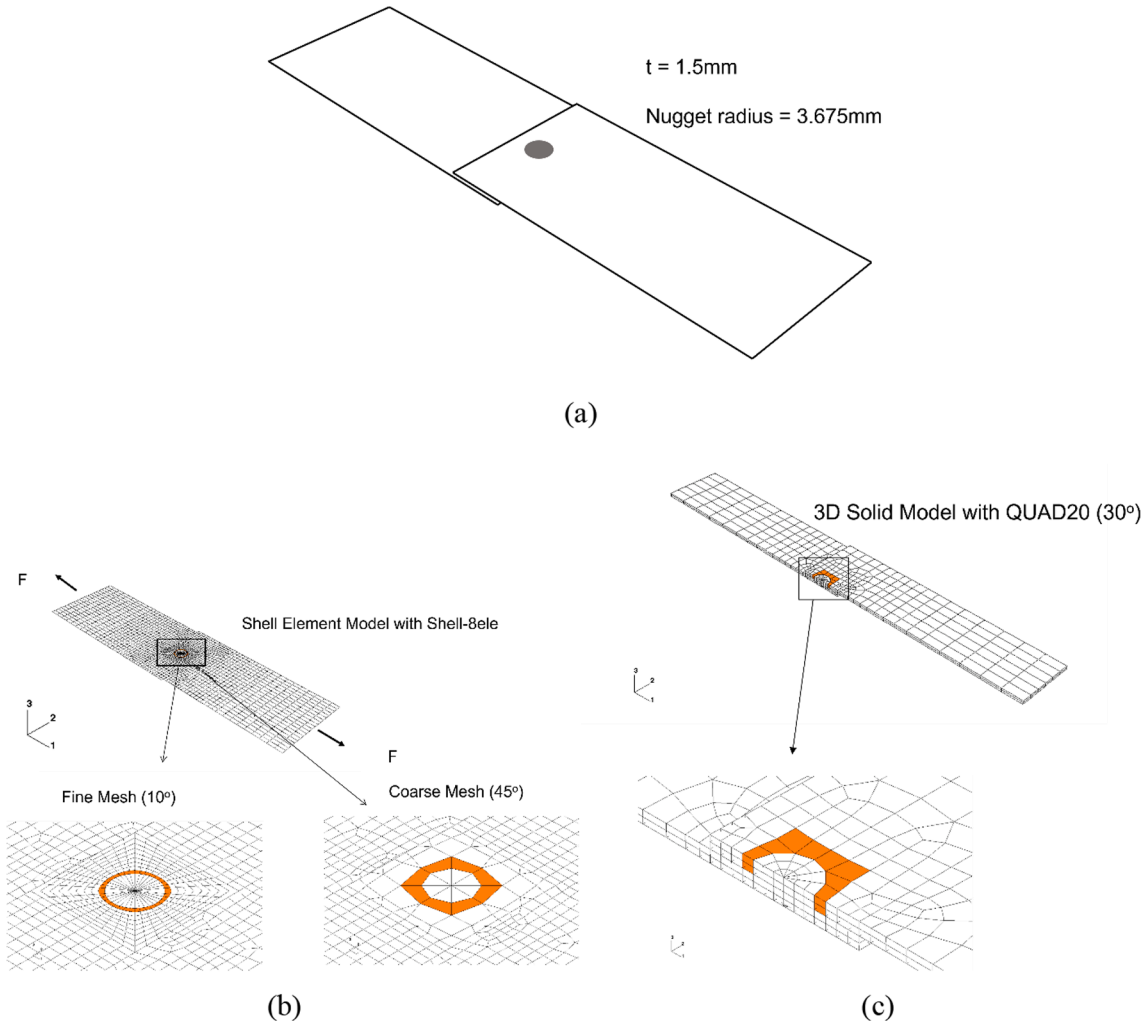

Fig. 4. A lap-shear spot-welded test specimen modeled with different element sizes and element types: (a) specimen overall geometry, (b) shell element models, and (c) 3D solid element model [22].

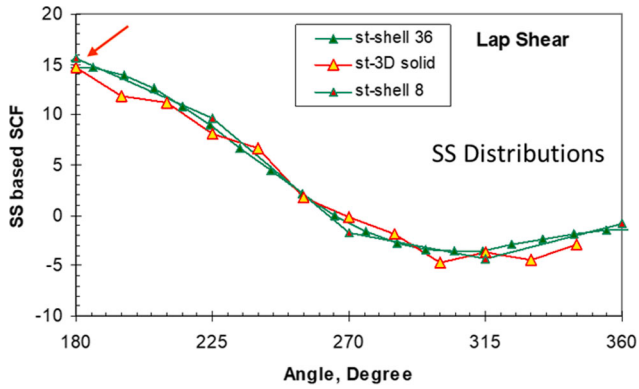

Fig. 5. Normalized structural stress (SS) distributions around the interface notch of lap shear test specimens, showing a good element size and type insensitivity in structural stress calculation [22].

the weld nugget area. Therefore, even for some laboratory test components with only several spot welds, for example, the modified H-shear components in Fig. 1, the efforts for their FE models with the explicit representation of spot welds involved can be significant, particularly in view of a couple of thousands of spot welds being used in a car body structures. Thus, a reliable and simplified mesh-insensitive structural stress method is needed for modeling spot-welded structures.

2.2. Coarse-Mesh hybrid structural stress method

In this section, a coarse-mesh hybrid structural stress method is presented. The method differs from the direct method described above in the following manner, as illustrated in Fig. 6:

(a) Model each spot weld with a single circular beam element with the beam cross-section diameter being the same as the spot weld it represents
(b) Extract nodal forces and nodal moments around a rectangular domain formed by a group of four shell elements connected at the center point by the beam element representing the spot weld
(c) Decompose the nodal forces and moments into a set of simple elementary loading modes for which analytical solutions are available
(d) Combine the solutions obtained by all elementary loading-mode based analytical solutions through superposition to obtain the final structural stress solution for each spot weld of interest.

Without losing generality, the procedure details described above can be more clearly illustrated by considering a spot weld location in a

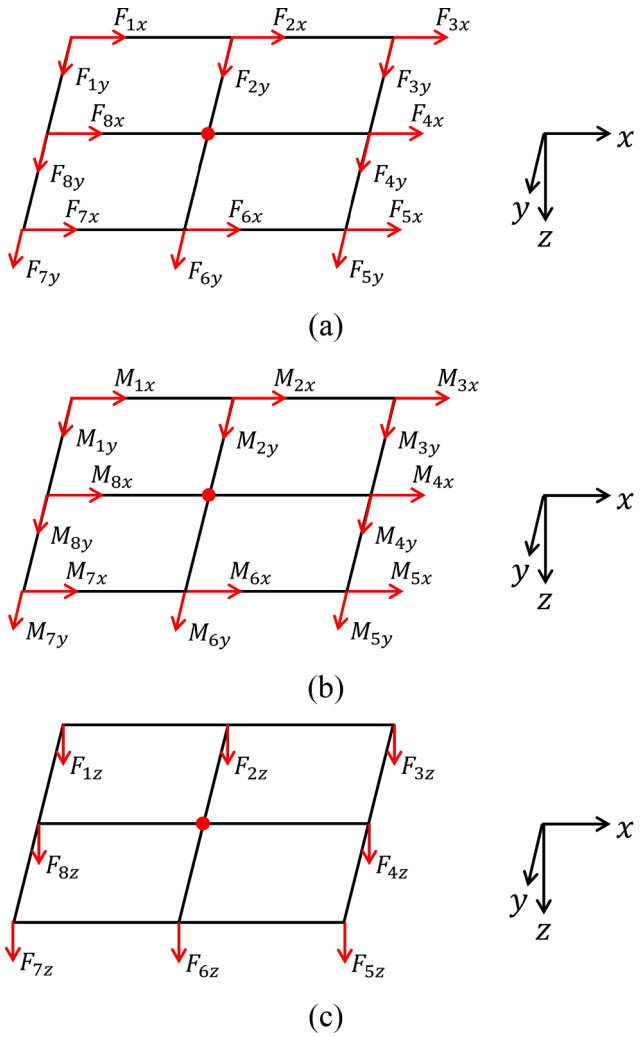

Fig. 7. (a) The in-plane nodal forces (F_x and F_y), (b) nodal moments (M_x and M_y), and (c) out-of-plane nodal force (F_z) at the eight nodes around spot weld.

component, as shown in Fig. 6. A pre-defined square-shaped domain formed by a group of shell elements (a total of four in the current case) is used for extracting nodal forces and nodal moments along the eight edge nodes, which are available after completion of a FE analysis of the structure. Note that the spot weld is centered at the mid-position of the square domain, as shown in Fig. 6. Fig. 7 shows the nodal forces and nodal moments at the eight nodal points around the edge of the square

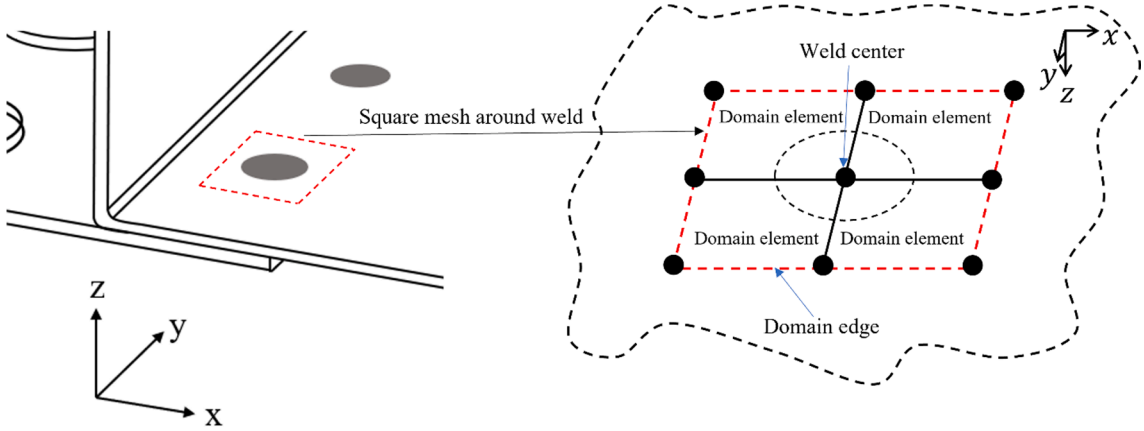

Fig. 6. The square domain around weld in multiple spot-welded structures.

Table 1
The procedures of nodal forces decomposition with respect to available analytical stress solutions.

Input	Nodal forces/moments at coarse mesh	Analytical solutions	Output
FE model with coarse mesh	In-plane nodal forces	Shear (E1, E3) Tension (E2, E4)	Radial structural stress σ_{rr}
	Nodal moments	Center bending (E5, E7) Counter bending (E6, E8)	
	Out-of-plane nodal forces	Open force (E9, E13) Center bending (E11, E12, E15, E16) Cross counter bending (E10, E14)	

element domain containing the spot weld modeled as a beam element. The Cartesian coordinate system X-Y-Z is also shown in this figure. The nodal forces and nodal moments can be separated into three categories: in-plane nodal forces (F_x and F_y), as shown in Fig. 5a, nodal moments (M_x and M_y), as shown in Fig. 5b, and out-of-plane nodal forces (F_z), as shown in Fig. 5c. Among these nodal forces and moments,F_x,F_y,F_z, M_x and M_y are of interest for further consideration in the coarse-mesh hybrid structural stress method, while the nodal moment M_z around the Z axis will not be considered further since previous investigations have shown that its effect is negligible for most structural applications [16].

With the nodal forces and nodal moments at the eight nodal points around spot weld, the decomposition-superposition procedure can be used to calculate the radial structural stress σ_{rr} with respect to available analytical solutions [9,16,17]. The details of the decomposition-superposition procedure with respect to available analytical solutions are presented in Appendix A. Table 1 summarizes the calculation flow of the decomposition-superposition procedure. In the decomposition step, the in-plane nodal forces are decomposed into four cases E1, E2, E3, and E4 corresponding to Fig. A1 with respect to the analytical solutions of the plate with a rigid inclusion under shear and tension forces. The nodal moments are decomposed into four cases E5, E6, E7, and E8 corresponding to Fig. A2 with respect to the analytical solutions of the plate with a rigid inclusion under center bending and counter bending moments. The out-of-plane nodal forces are decomposed into the cases E9 to E16. E9 and E13 correspond to the top figures in Fig. A3 and Fig. A5 with respect to the analytical solutions of the plate with a rigid inclusion under opening force. Cases E10 and E14 correspond to the bottom figures in Fig. A3 and Fig. A5 with respect to the analytical solutions of the plate with a rigid inclusion under cross counter bending moments. Cases E11, E12, E15, and E16 correspond to Fig. A4 and Fig. A6 with respect to the analytical solutions of the plate with a rigid inclusion under center bending moments. It should be mentioned that the available analytical solutions of the plate with a rigid inclusion under tension force, shear force, center bending moment, counter bending moment, opening force, and cross counter bending moments are presented in Sung and Pan [17] and Lin and Pan [9,16]. In the superposition procedure as presented in Section 2.3, the radial structural stresses $(\sigma_{rr})_{Ei}$ (i = 1-16) calculated from the cases E1 to E16 are added up to the total radial structural stresses σ_{rr} which will be used for the fatigue life analyses and fatigue data correlation in Section 4.

2.3. Decomposed loading cases and analytical solutions

As presented in Appendix A, the nodal forces and nodal moments at the 8 nodal points situated on the square domain edge can be decomposed into a total of 16 simple loading conditions with respect to which closed-form analytical solutions are available [9,16,17]. They are summarized below, based on 3 broad categories of loading cases against nugget interface notch, which are in-plane forces (shear and tension), moments (center bending and counter bending), and interfacial notch opening (out-of-plane forces and moments caused by out-of-plane forces).

2.3.1. In-Plane shear and In-Plane tension

The in-plane shear and in-plane tension along the x direction, Case E1 and Case E2, respectively, are listed as Eq. (5) and Eq. (6) according to Sung and Pan [17]:

$$(\sigma_{rr})_{E1}=\frac{(F_{Ax}+F_{Cx})}{4bt}\frac{\cos\theta}{S\pi\gamma^3}\{4[\gamma^2(1+\nu)(3+\nu)-\alpha^2(1+\nu)^2]+2(\pi-\nu-1)[\gamma^4(1+\nu)+\alpha^4(3-\nu)]+\alpha^2\gamma^2[\gamma^2(1+\nu)^2+\alpha^2(9-\nu^2)]\} \tag{5}$$

where $S=4(1+\nu)+\alpha^4(3-\nu)$,$\alpha=\frac{a}{b}$, and $\gamma=\frac{r}{b}$, a is the radius of spot weld and b is the coarse-mesh element size.

$$(\sigma_{rr})_{E2}=\frac{(F_{Cx}-F_{Ax})}{8bt}\frac{1}{\gamma^4WY}\{Y[(-3+\nu)(3-4\gamma^2)(1+\nu)\alpha^8+4\gamma^4(\nu^2+3)\alpha^6-3(1+\nu)^2(1+\gamma^4)\alpha^4+4\gamma^2(1+\nu)^2\alpha^2-\gamma^4(1+\nu)(-3+\nu)]cos2\theta-\gamma^2W[\alpha^2(\nu-1)-\gamma^2(1+\nu)]\} \tag{6}$$

where $W=(1+\alpha^8)(1+\nu)(3-\nu)+2\alpha^2(2-3\alpha^2)(1+\nu)^2+4\alpha^6(3+\nu^2)$ and $Y=(1+\nu)+\alpha^2(1-\nu)$.

The in-plane shear and in-plane tension along the y direction, Case E3 and Case E4, respectively, are listed as Eq. (7) and Eq. (8) as given by Sung and Pan [17]:

$$(\sigma_{rr})_{E3}=\frac{(F_{By}+F_{Dy})}{4bt}\frac{\sin\theta}{S\pi\gamma^3}\{4[\gamma^2(1+\nu)(3+\nu)-\alpha^2(1+\nu)^2]+2(\pi-\nu-1)[\gamma^4(1+\nu)+\alpha^4(3-\nu)]+\alpha^2\gamma^2[\gamma^2(1+\nu)^2+\alpha^2(9-\nu^2)]\} \tag{7}$$

$$(\sigma_{rr})_{E4}=\frac{(F_{Dy}-F_{By})}{8bt}\frac{1}{\gamma^4WY}\{-Y[(-3+\nu)(3-4\gamma^2)(1+\nu)\alpha^8+4\gamma^4(\nu^2+3)\alpha^6-3(1+\nu)^2(1+\gamma^4)\alpha^4+4\gamma^2(1+\nu)^2\alpha^2-\gamma^4(1+\nu)(-3+\nu)]cos2\theta-\gamma^2W[\alpha^2(\nu-1)-\gamma^2(1+\nu)]\} \tag{8}$$

2.3.2. Center bending and counter bending

The center bending and counter bending along the y direction, Case E5 and Case E6, respectively, are listed as Eq. (9) and Eq. (10), according to Sung and Pan [17]:

$$(\sigma_{rr})_{E5}=\frac{(M_{Cy}+M_{Ay})}{2b}\frac{3}{t^2}\frac{\cos\theta}{Z\pi\gamma^3}\{4(3+\nu)[\gamma^2(1+\nu)+\alpha^2(1-\nu)]+2(\pi-\nu+1)[\gamma^4(3+\nu)+\alpha^4(1-\nu)]-\alpha^2\gamma^2(1-\nu)[\gamma^2(3+\nu)-\alpha^2(1+\nu)]\} \tag{9}$$

where

$$Z=4(3+\nu)+\alpha^4(1-\nu)$$

$$(\sigma_{rr})_{E6}=\frac{9(M_{Cy}-M_{Ay})}{4bt^2}\frac{1}{\gamma^4 XY}\{\gamma^2[\gamma^2(1+\nu)+\alpha^2(1-\nu)]\left[4\alpha^2(1+\nu)+(\alpha^4+1)^2(1-\nu)\right] +Y[\alpha^8(1-\nu)+\alpha^4(1-\nu)(3-\gamma^4)+4\alpha^2\gamma^2(\gamma^4+\nu)+\gamma^4(1-\nu)]cos2\theta \tag{10}$$

where $X=(1-\nu)(\alpha^8+3)+4\alpha^2(3+\nu)$ and $Y=(1+\nu)+\alpha^2(1-\nu)$.

Similarly, the center bending and counter bending along the x direction, Case E7 and Case E8, respectively, are listed as Eq. (11) and Eq. (12), according to Sung and Pan [17]:

$$(\sigma_{rr})_{E7}=\frac{-(M_{Bx}+M_{Dx})}{2b}\frac{3}{t^2}\frac{\sin(\theta)}{Z\pi\gamma^3}\{4(3+\nu)[\gamma^2(1+\nu)+\alpha^2(1-\nu)] +2(\pi-\nu+1)[\gamma^4(3+\nu)+\alpha^4(1-\nu)]-\alpha^2\gamma^2(1-\nu)[\gamma^2(3+\nu)-\alpha^2(1+\nu)]\} \tag{11}$$

$$(\sigma_{rr})_{E8}=\frac{-9(M_{Dx}-M_{Bx})}{4bt^2\gamma^4 XY}\{\gamma^2[\gamma^2(1+\nu)+\alpha^2(1-\nu)]\left[4\alpha^2(1+\nu)+(\alpha^4+1)^2(1-\nu)\right] -Y[\alpha^8(1-\nu)+\alpha^4(1-\nu)(3-\gamma^4)+4\alpha^2\gamma^2(\gamma^4+\nu)+\gamma^4(1-\nu)]cos2\theta \tag{12}$$

2.3.3. Interfacial notch opening

The opening forces along z direction, Case E9, is listed as Eq. (13), according to Lin and Pan [16]:

$$(\sigma_{rr})_{E9}=\frac{-3(F_{8z}+F_{4z}+F_{2z}+F_{6z})}{2\pi r^2 t^2[a^2(-1+\nu)-b'^2(1+\nu)]}\{a^2(b'^2-r^2)(-1+\nu) +b'^2(1+\nu)[a^2(-1+\nu)-r^2(1+\nu)]ln(b'/a) +r^2[b'^2(1+\nu)^2-a^2(-1+\nu^2)]ln(r/a) \tag{13}$$

where the equivalent radius $b'=\frac{2b}{\sqrt{\pi}}$ is used based on the equivalent circular plate model as suggested by Lin and Pan [16].

The cross counter bending, Case E10, is listed as Eq. (14), according to Lin and Pan [9] and Sung and Pan [17]:

$$(\sigma_{rr})_{E10}=\frac{-9(F_{8z}+F_{4z}-F_{2z}-F_{6z})}{8t^2\gamma'^4X'Y'}\{\gamma'^2[\gamma'^2(1+\nu) +\alpha'^2(1-\nu)]\left[4\alpha'^2(1+\nu)+(\alpha'^4+1)^2(1-\nu)\right] +Y'[\alpha'^8(1-\nu)+\alpha'^4(1-\nu)(3-\gamma'^4)+4\alpha'^2\gamma'^2(\gamma'^4+\nu)+\gamma'^4(1-\nu)]cos2\theta\} +\frac{9(F_{8z}+F_{4z}-F_{2z}-F_{6z})}{8t^2\gamma'^4X'Y'}\{\gamma'^2[\gamma'^2(1+\nu) +\alpha'^2(1-\nu)]\left[4\alpha'^2(1+\nu)+(\alpha'^4+1)^2(1-\nu)\right] -Y'[\alpha'^8(1-\nu)+\alpha'^4(1-\nu)(3-\gamma'^4)+4\alpha'^2\gamma'^2(\gamma'^4+\nu)+\gamma'^4(1-\nu)]cos2\theta\} \tag{14}$$

where $X'=(1-\nu)(\alpha'^8+3)+4\alpha'^2(3+\nu)$, $Y'=(1+\nu)+\alpha'^2(1-\nu)$, $\gamma'=\frac{\sqrt{2}r}{b}$, and $\alpha'=\frac{\sqrt{2}a}{b}$.

The center bending caused by the out-of-plane nodal forces along the y and x directions, Case E11 and Case E12, respectively, are listed as Eq. (15) and Eq. (16), according to Sung and Pan [17]:

$$(\sigma_{rr})_{E11}=\frac{(F_{8z}-F_{4z})}{2}\frac{3}{t^2}\frac{\cos\theta}{Z\pi\gamma^3}\{4(3+\nu)[\gamma^2(1+\nu)+\alpha^2(1-\nu)] +2(\pi-\nu+1)[\gamma^4(3+\nu)+\alpha^4(1-\nu)]-\alpha^2\gamma^2(1-\nu)[\gamma^2(3+\nu)-\alpha^2(1+\nu)]\} \tag{15}$$

$$(\sigma_{rr})_{E12}=\frac{-(F_{6z}-F_{2z})}{2}\frac{3}{t^2}\frac{\sin(\theta)}{Z\pi\gamma^3}\{4(3+\nu)[\gamma^2(1+\nu)+\alpha^2(1-\nu)] +2(\pi-\nu+1)[\gamma^4(3+\nu)+\alpha^4(1-\nu)]-\alpha^2\gamma^2(1-\nu)[\gamma^2(3+\nu)-\alpha^2(1+\nu)]\} \tag{16}$$

The opening forces along z direction for the plate with the rotation of $\frac{\pi}{4}$, Case E13, is listed as Eq. (17), according to Lin and Pan [16]:

$$(\sigma_{rr})_{E13}=\frac{-3(F_{7z}+F_{3z}+F_{1z}+F_{5z})}{2\pi r^2 t^2[a^2(-1+\nu)-b''^2(1+\nu)]}\{a^2(b''^2-r^2)(-1+\nu) +b''^2(1+\nu)[a^2(-1+\nu)-r^2(1+\nu)]ln(b''/a) +r^2[b''^2(1+\nu)^2-a^2(-1+\nu^2)]ln(r/a)\} \tag{17}$$

where

$$b'' = \frac{2\sqrt{2}b}{\sqrt{\pi}}$$

The cross counter bending for the plate with the rotation of $\frac{\pi}{4}$, Case E14, is listed as Eq. (18), according to Lin and Pan [9] and Sung and Pan [17]:

$$\begin{aligned}(\sigma_{rr})_{E14} = &\frac{-9(F_{1z}+F_{5z}-F_{3z}-F_{7z})}{8t^2\gamma^4 XY}\{\gamma^2[\gamma^2(1+\nu)\\ &+\alpha^2(1-\nu)]\left[4\alpha^2(1+\nu)+(\alpha^4+1)^2(1-\nu)\right]\\ &+Y[\alpha^8(1-\nu)+\alpha^4(1-\nu)(3-\gamma^4)+4\alpha^2\gamma^2(\gamma^4+\nu)+\gamma^4(1-\nu)]sin2\theta\}\\ &+\frac{9(F_{1z}+F_{5z}-F_{3z}-F_{7z})}{8t^2\gamma^4 XY}\{\gamma^2[\gamma^2(1+\nu)\\ &+\alpha^2(1-\nu)]\left[4\alpha^2(1+\nu)+(\alpha^4+1)^2(1-\nu)\right]\\ &-Y[\alpha^8(1-\nu)+\alpha^4(1-\nu)(3-\gamma^4)+4\alpha^2\gamma^2(\gamma^4+\nu)+\gamma^4(1-\nu)]sin2\theta\}\end{aligned} \tag{18}$$

The center bending and counter bending caused by out-of-plane nodal forces for the plate with the rotation of $\frac{\pi}{4}$, Case E15 and Case E16, respectively, are listed as Eq. (19) and Eq. (20), according to Sung and Pan [17]:

$$\begin{aligned}(\sigma_{rr})_{E15} = &\frac{(F_{7z}-F_{3z})}{2}\frac{3}{t^2}\frac{(\cos\theta-\sin\theta)}{Z^{`}\pi\gamma^{``3}}\{4(3+\nu)[\gamma^{``2}(1+\nu)+\alpha^{``2}(1-\nu)]\\ &+2(\pi-\nu+1)[\gamma^{``4}(3+\nu)+\alpha^{``4}(1-\nu)]\\ &-\alpha^{``2}\gamma^{``2}(1-\nu)[\gamma^{``2}(3+\nu)-\alpha^{``2}(1+\nu)]\}\end{aligned} \tag{19}$$

$$\begin{aligned}(\sigma_{rr})_{E16} = &\frac{-(F_{5z}-F_{1z})}{2}\frac{3}{t^2}\frac{(\cos\theta+\sin\theta)}{Z^{`}\pi\gamma^{``3}}\{4(3+\nu)[\gamma^{``2}(1+\nu)+\alpha^{``2}(1-\nu)]\\ &+2(\pi-\nu+1)[\gamma^{``4}(3+\nu)+\alpha^{``4}(1-\nu)]\\ &-\alpha^{``2}\gamma^{``2}(1-\nu)[\gamma^{``2}(3+\nu)-\alpha^{``2}(1+\nu)]\}\end{aligned} \tag{20}$$

where $Z^{`} = 4(3+\nu)+\alpha^{``4}(1-\nu)$, $\gamma'' = \frac{r}{\sqrt{2}b}$, and $\alpha'' = \frac{a}{\sqrt{2}b}$.

3. Applications in modeling of multiple Spot-Welded specimens

3.1. Lap-Shear specimen with double spot welds in series

Lap-shear specimens with double spot welds are used to examine the accuracy of the proposed coarse-mesh hybrid structural stress method. Because there are no applicable closed-form solutions in literature for the lap-shear specimens with double spot welds, two approximate analytical methods (referred to hereafter as Methods 1 and 2) for making use of existing closed-form solutions are devised here for comparison with both the hybrid structural stress method as well as the direct method. The first analytical method (Method 1) takes into account of both the through-nugget forces and moments (in-plane shear and center bending) and the self-balanced forces and moments (in-plane tension and counter bending), as discussed in Lin and Pan [16]. The second analytical method (Method 2) only takes into account of the through-nugget forces and moments, representing the approach adopted by industry based on the work by Rupp et al. [6].

The spot weld studied in this investigation has a nugget radius a of 3.5 mm. Fig. 8 shows the schematic of a lap-shear specimen with double spot welds in series. The width of the specimen B is 38 mm, the distance between two spot welds L is 38 mm, and the length of the overlap region W is 76 mm. The corresponding FE models for the direct method and the coarse-mesh hybrid structural stress method are shown in Fig. 9a and b, respectively. In Fig. 9a, the two welds are explicitly modeled as the two circular regions with the MPC beam constraints [30]. In Fig. 9b, the same two welds are simply represented by two linear beam elements at their center locations. The boundary conditions of the lap-shear specimen with double spot welds in series are similar to those of the lap-shear specimen with single weld shown in Fig. B1a and Fig. B2a and are not elaborated further here. To examine the mesh-insensitivity of the hybrid method in structural stress determination, three mesh sizes with b/a of 2.72, 3.39, and 4.07 are used, as shown in Fig. 10. Here, a is the radius of the weld nugget and b is the element size around the spot weld.

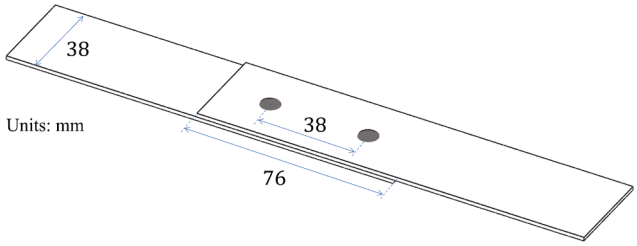

Fig. 8. The schematics of a lap-shear specimen with double spot welds in series.

Fig. 11a and b show the normalized radial structural stress σ_{rr} (by applied remote nominal stress) around weld nugget edge notch tip of 1st and 2nd spot welds, respectively. In the figures, the black solid lines with circular markers represent the reference solution obtained by means of the direct structural stress method. The black dashed lines represent the solution obtained by using Method 1 (labeled as "Analytical Solution 1" in Fig. 11a). The black dash-dotted lines represent the solutions obtained by using Method 2 ("Analytical Solution 2"). The red, blue, and green dashed lines represent the results obtained from the hybrid method developed in this study, corresponding to three different element sizes. As shown in Fig. 11, the radial structural stress σ_{rr} obtained from the coarse-mesh hybrid structural stress method agrees very well with those obtained using the direct method, proving the method's mesh-size insensitivity.

The results in Fig. 11 also show that Method 2 ("Analytical Solution 2") only taking into account of through-nugget forces and moments cannot capture the radial structural stresses σ_{rr} adequately, as also discussed in Lin and Pan [16]. Method 1 ("Analytical Solution 1") which takes into account of both through-nugget and self-balanced forces and moments offers a reasonable estimation of the radial structural stress σ_{rr} for the 2nd spot weld, but not for the 1st spot weld.

3.2. Lap-Shear specimen with double spot welds in parallel

Fig. 12 shows the schematics of the lap-shear specimen with double spot welds in parallel. The width of the specimen B is 76 mm, the distance between spot welds L is 24.5 mm, and the length of overlap region W is 38 mm. The corresponding FE models for both the direct method and the hybrid structural stress method are shown in Fig. 13a and b, respectively. Fig. 13a shows the welds explicitly modeled as two circular regions with the MPC beam constraints [30]. In Fig. 13b, the welds are simply represented by two beam elements. The boundary conditions of

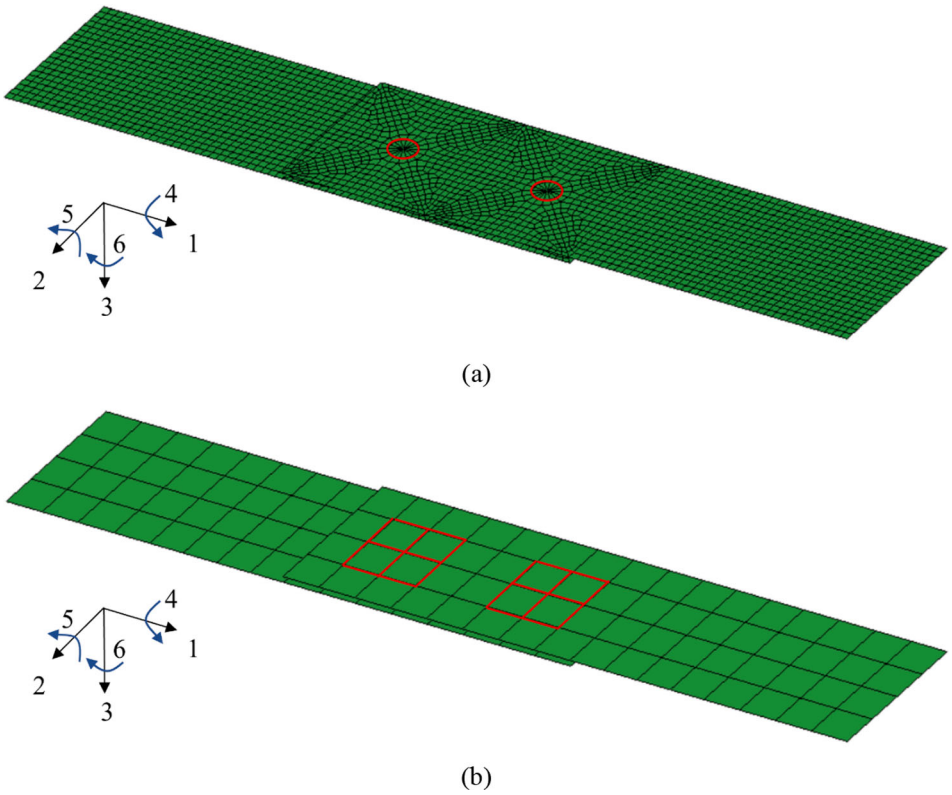

Fig. 9. The FE models of a lap-shear specimen with two spot welds in series using (a) direct structural stress method and (b) coarse-mesh hybrid structural stress method.

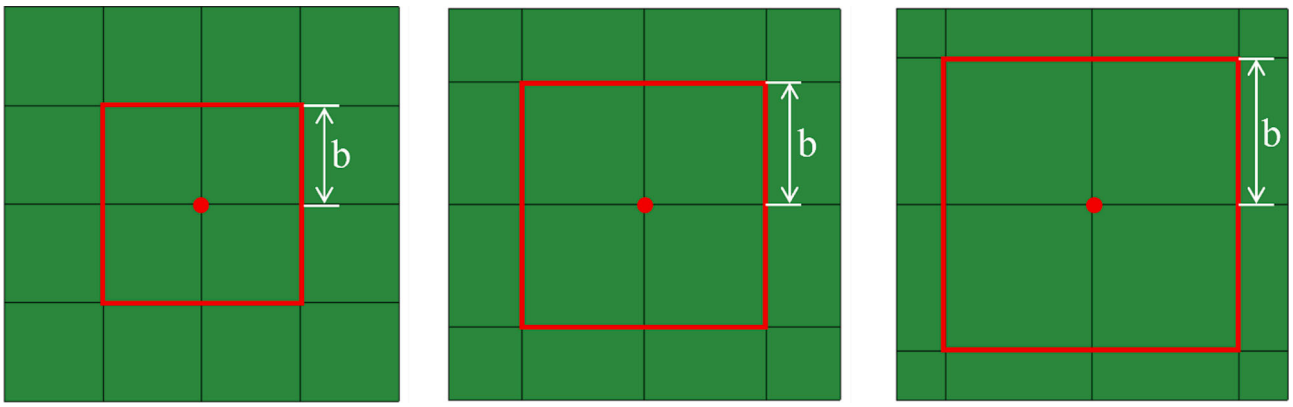

Fig. 10. The close-up view of the three coarse mesh sizes near spot weld with the b/a of 2.72, 3.39, and 4.07 from left to right.

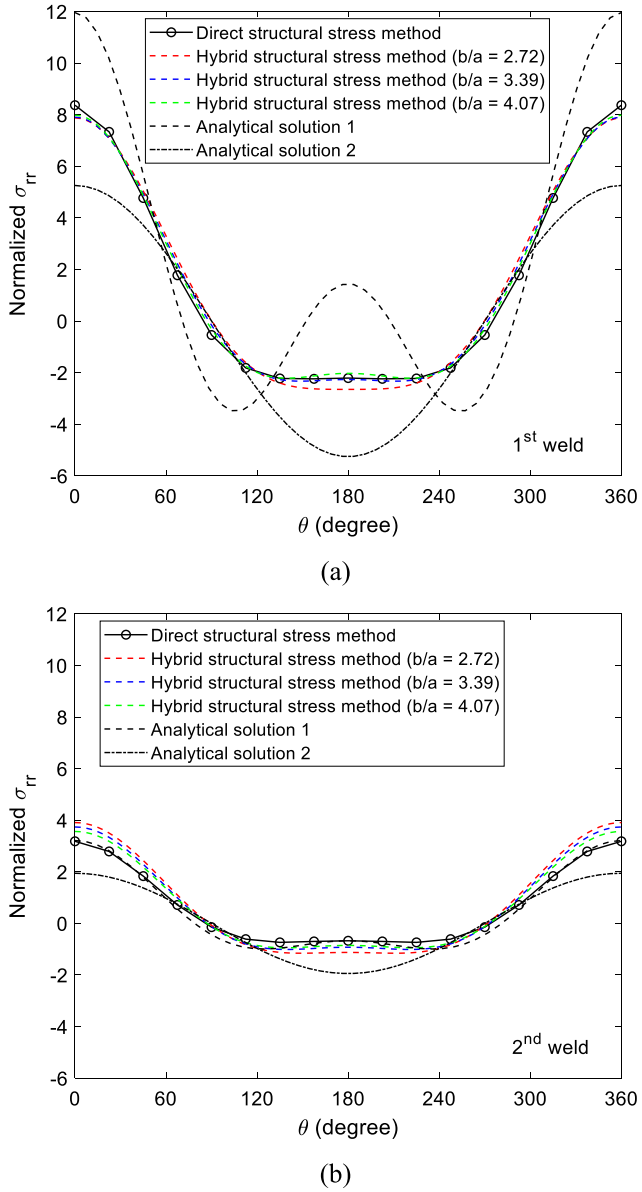

Fig. 11. The computational radial structural stress distributions around weld nugget edge of (a) 1st weld and (b) 2nd weld in the lap-shear specimen with double spot welds in series.

the lap-shear specimens with double spot welds in parallel are similar to those for the lap-shear specimen with single weld shown in Fig. B1a and Fig. B2a and are not elaborated here.

Due to symmetry, only one-half of the lap-shear specimen with double spot welds in parallel is considered. Fig. 14 shows the normalized radial structural stress σ_{rr} around the weld nugget edge. The results obtained from the hybrid structural stress method agree very well with those obtained using the direct structural stress method. The results in Fig. 14 also prove Method 2 ("Analytical Solution 2") only taking into account of through-nugget forces and moments cannot offer an adequate

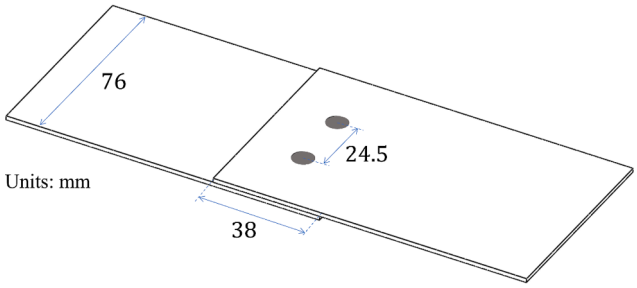

Fig. 12. The schematics of a lap-shear specimen with double spot welds in parallel.

estimation of the radial structural stresses σ_{rr}, as also shown in Lin and Pan [16]. Furthermore, Method 1 (Analytical Solution 1) with both through-nugget and self-balanced forces and moments fails to correctly predict the radial structural stress σ_{rr} around weld nugget edge in this case. The details of the approximate analytical solutions will be discussed in detail in a later section.

3.3. Fatigue test data correlation

The experimental data in terms of nominal stress range vs cycle to failure for the coach-peel with one weld and lap-shear with one or three welds obtained from Zhang et al. [19] were shown in Fig. 15a. Here, nominal stress range is defined as applied force range divided by the loaded sheet cross-section area. As expected, the nominal stress range vs cycle to failure fatigue test data from different types of specimens are far apart from one another, particularly between coach peel and lap shear specimens. Therefore, as is well known, nominal stress based methods do not offer fatigue test data transferability. Once the structural stress for each type of specimens is computed using the hybrid method presented in the previous section is used, the structural stress range parameter offers an effective data correlation, as shown in Fig. 15b, regardless of specimen types. The details of the coarse-mesh hybrid structural calculation procedure are given in Appendix B. The results in Fig. 15b imply that the hybrid structural stress method not only provides reliable structural stress results with a very coarse finite element mesh (e.g., see Fig. 13), but also enables fatigue test data transferability among different specimen types and loading conditions, as illustrated in Fig. 15.

4. Discussions

4.1. Mesh-Size insensitivity and multiple weld interactions

The mesh insensitivity exhibited in the structural stress results obtained by the hybrid method is overall satisfactory, as discussed in Section 3.1 for the lap-shear specimen with double spot welds in series and in Appendix B for both the lap-shear and coach-peel specimens with single spot weld. It is observed from Fig. 10 and Fig. B3 that a smaller mesh size tends to result in a somewhat lower maximum radial structural stress $\sigma_{rr_{max}}$, which is likely due to the limitations inherent in the available analytical solutions adopted from Sung and Pan [17]. Sung and Pan [17] presented that the ratio of b/a should be larger than 5 for ensuring the accuracy of the analytical solutions.

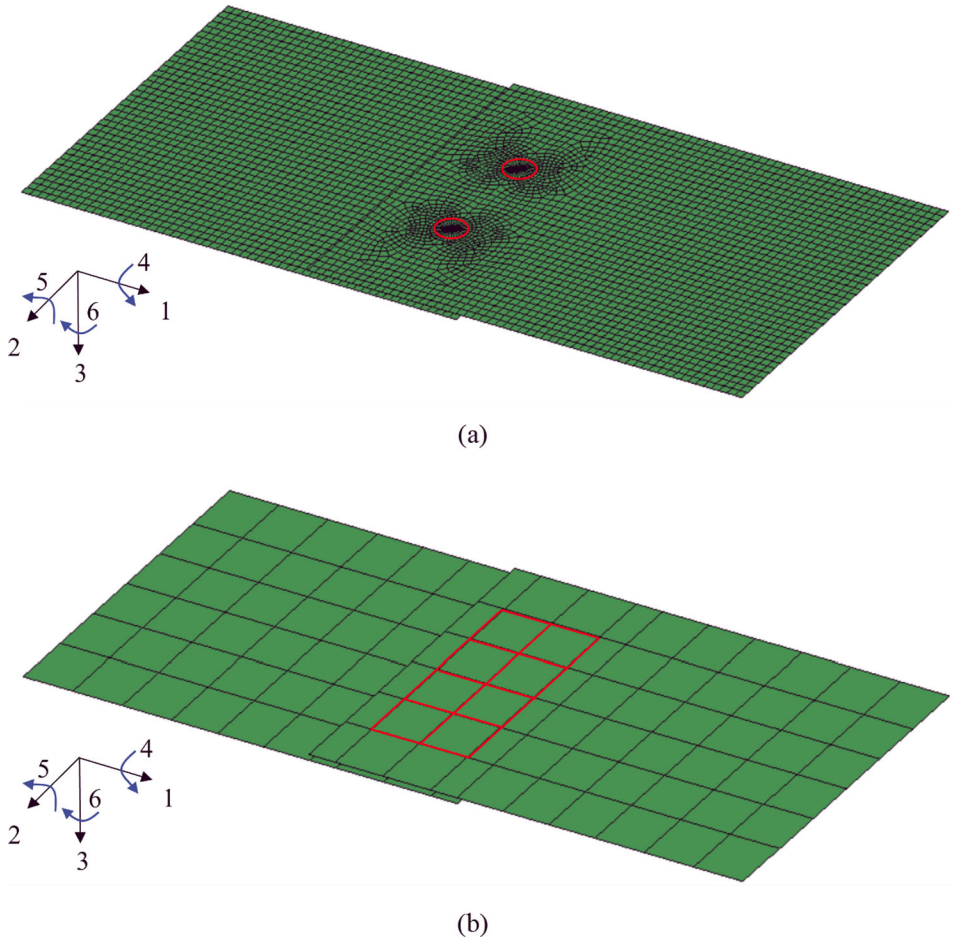

Fig. 13. The FE models of a lap-shear specimen with two spot welds in parallel using (a) direct structural stress method and (b) coarse-mesh hybrid structural stress method.

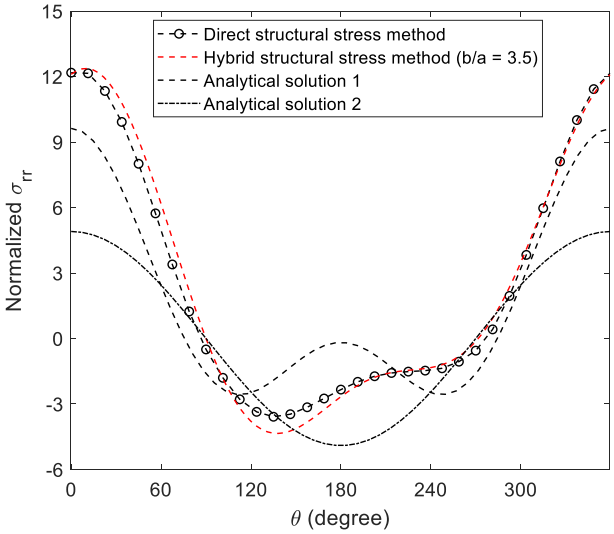

Fig. 14. The computational radial structural stress distribution around the weld nugget edge of the lap-shear specimen with double spot welds in parallel.

Based on the proposed hybrid structural stress method, the radial structural stress σ_{rr} distribution around the 2nd spot weld in the lap-shear specimen with double spot welds in series seems to show some noticeable discrepancies (see Fig. 11b), compared with the results as shown in Fig. 11a. This can be attributed to the inadequate representation of the deformation field around spot welds in such a coarse finite element model with each spot weld being modeled by a beam element. As a result, a single beam element simulating a spot weld is not capable of accurately representing the complex deformation characteristics around weld nugget, leading to the discrepancies in the structural stress results shown in Fig. 11b. Here, two aspects are worth noting: (a) The somewhat over-estimation in the structural stresses obtained by the hybrid method in Fig. 11b can be viewed as being conservative for engineering applications while offering a significant simplicity; (b) The structural stress results for the critical weld (the 1st weld in this case) of the two is sufficiently accurate. The latter is important since structural fatigue lives are governed by just a few critical welds, for which the hybrid method seems to work well.

To substantiate the above observations, the multi-spot-welded H-shear component shown in Fig. 1b is considered here, under the fatigue loading conditions described by Zhang et al. [19]. Indeed, the peak structural stress location at $\theta = 0^{\circ}, 360^{\circ}$ shows a more reasonable estimation than that at $\theta = 180^{\circ}$. It is worth noting that the predicted $\theta = 0^{\circ}, 360^{\circ}$ position is indeed consistent with the test results documented in [8,19]. It should be noted that the discrepancies around $\theta = 180^{\circ}$ shown in Fig. 16 are in the region of very low stress and therefore do not impact the fatigue life evaluation of structures in which only high stress regions dominate fatigue performance. To further improve the structural stress results around $\theta = 180^{\circ}$ shown in Fig. 16, a new finite element formulation by introducing sufficient deformation constraints around nugget edge may need to be explicitly considered, which is beyond the current scope of study as far as a hybrid structural stress method is concerned.

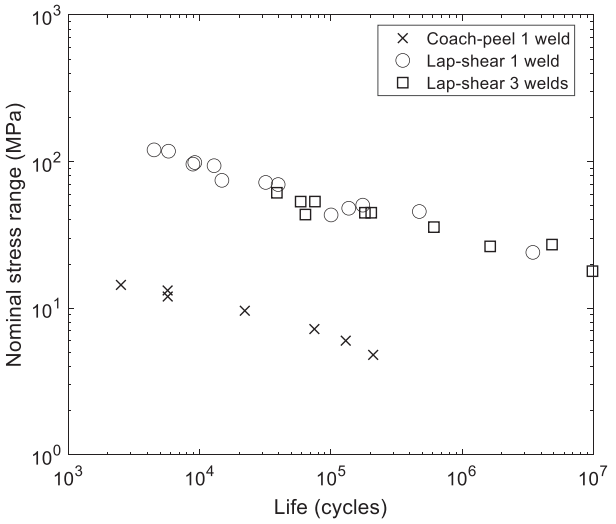

(a)

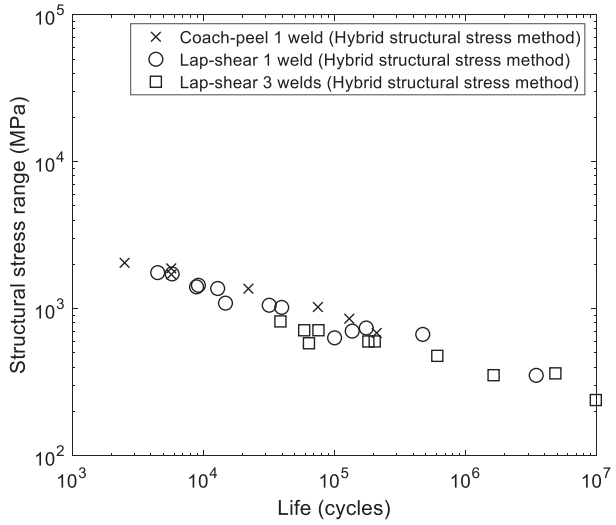

(b)

Fig. 15. Fatigue test data correlation: (a) Nominal stress range vs life and (b) correlation of structural stress range vs life of the lap-shear specimens with 1 or 3 welds and coach-peel specimens with 1 weld.

4.2. Limitations in existing analytical stress solutions

For the lap-shear specimens with double spot welds in series and in parallel examined in Section 3. Approximate analytical stress solutions are used to compare with the results obtained from the coarse-mesh hybrid structural stress method. Fig. 17 shows the side view of the lap-shear specimen with double spot welds in series and the free body diagrams (FBDs) for the 1st spot weld and 2nd spot weld. As shown in Fig. 17a, the 1st spot weld is close to the applied force and the 2nd spot weld is close to the free edge. In FBDs shown in Fig. 15b, F_1 and M_1 are the force and moment through the upper part of 1st spot weld in top plate or the lower part of 2nd spot weld in bottom plate due to symmetry. Similarly, F_2 and M_2 are the force and moment through the upper part of 2nd spot weld in top plate or the lower part of 1st spot weld in bottom plate due to symmetry. Also, the force balance and moment balance require:

$$F_1 + F_2 = F \tag{21}$$

$$M_1 + M_2 = M = \frac{Ft}{2} \tag{22}$$

where t is the plate thickness, F is the applied force and M is the through-nugget moment from the applied force F.

The FBDs of the plates with 1st spot weld and 2nd spot weld are shown in Fig. 18a and b, respectively. The decomposition processes to the cases of shear force, tension force, center bending moment, and counter bending moment are also shown in Fig. 18 for the plates with 1st spot weld and 2nd spot weld. The decomposition processes and the corresponding analytical solutions are similar to those in Zhang et al. [31] for the lap-shear specimen with single spot weld as shown in Fig. 19. When calculating the total radial structural stress distribution for 1st spot weld at upper plate, replace $(F_{Ax} + F_{Cx})/2$ with $F/4$ in Eq. (5) for shear case, replace $(F_{Cx} - F_{Ax})/2$ with $3F/4$ in Eq. (6) for tension case, replace $(M_{Cy} + M_{Ay})/2$ with $(M - M_2)/2$ in Eq. (9) for center bending case, and replace $(M_{Cy} - M_{Ay})/2$ with $(M + M_2)/2$ in Eq. (10) for counter bending case. When calculating the total radial structural stress distribution for 2nd spot weld at upper plate, replace $(F_{Ax} + F_{Cx})/2$ with $F/4$ in Eq. (5) for shear case, replace $(F_{Cx} - F_{Ax})/2$ with $F/4$ in Eq. (6) for tension case, replace $(M_{Cy} + M_{Ay})/2$ with $M_2/2$ in Eq. (9) for center bending case, and replace $(M_{Cy} - M_{Ay})/2$ with $M_2/2$ in Eq. (10) for counter bending case. Finally, add all these radial structural stresses from the four cases discussed above. It should be mentioned that the b used in analytical solution 1 and analytical solution 2 is different compared with that used in hybrid structural stress method. In analytical solution 1 and analytical solution 2, b represents the half width of the plate. In coarse-mesh hybrid structural stress method, b represents the element size.

Fig. 20 shows the top view of the lap-shear specimen with double spot welds in parallel. Due to the lack of analytical solution, the analytical solution for the lap-shear specimen with single spot weld is adopted here as an approximation. The red square area in Fig. 18 shows the cut-out to apply the approximate analytical solution. As shown in Fig. 18, the nodal forces F_x and nodal moments M_y at the nodal points 1, 3, 4, 5, 7, and 8 are used to obtain the analytical stress solutions under self-balanced loading conditions, in-plane tension and counter bending as shown in Fig. 19. In order to obtain the accurate analytical stress solutions under resultant loading conditions, in-plane shear and center bending as shown in Fig. 17, the nodal forces $F_x = F/2$ and nodal moments $M_y = Ft/4$ at the weld are used. The details of the analytical stress solution for the lap-shear specimen with single spot weld can be found in Lin and Pan [16] and Zhang et al. [31].

The readers should realize that even for these simple laboratory specimens, the proposed approximate analytical stress solutions require tedious free body diagram analyses and also adopt the decomposition-superposition scheme to take account of the various loading conditions. It should be mentioned that, unlike the coarse-mesh hybrid structural stress method, the approximate analytical stress solutions here only consider the loading forces along the x direction and moments along the y direction. In addition, it should be pointed out, the approximate analytical stress solutions are not unique and different researchers may propose different solutions. For example, one may approximate the lap-shear specimen with double spot welds in parallel as two simple lap-shear specimens as shown in Fig. 21 for the use of the analytical solutions presented in Zhang et al. [31].

It also needs to emphasize that it is impossible to derive the accurate approximate analytical stress solutions for the complicated spot-weld structures like the modified H-shear component in Fig. 1b. To solve the difficulty of applying approximate analytical stress solution in complex spot-weld structures is the intention of the proposed coarse-mesh hybrid structural stress method.

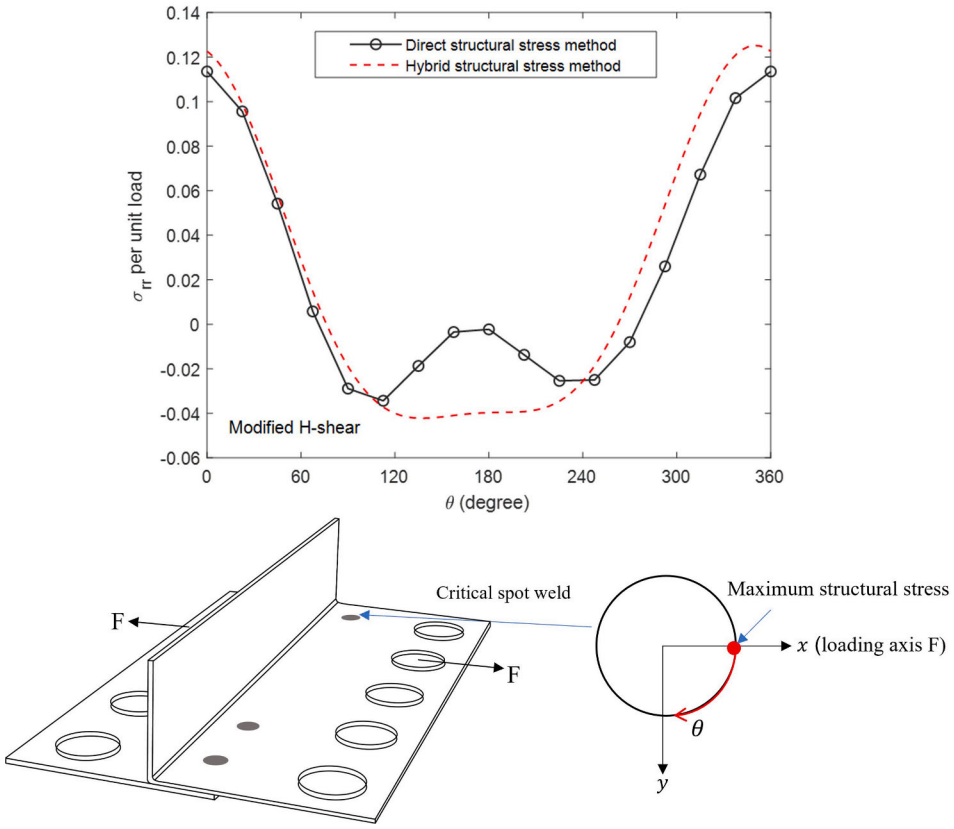

Fig. 16. Comparison of direct and hybrid structural stress results (normalized by a unit load of "F") around the critical spot weld in modified H-shear component.

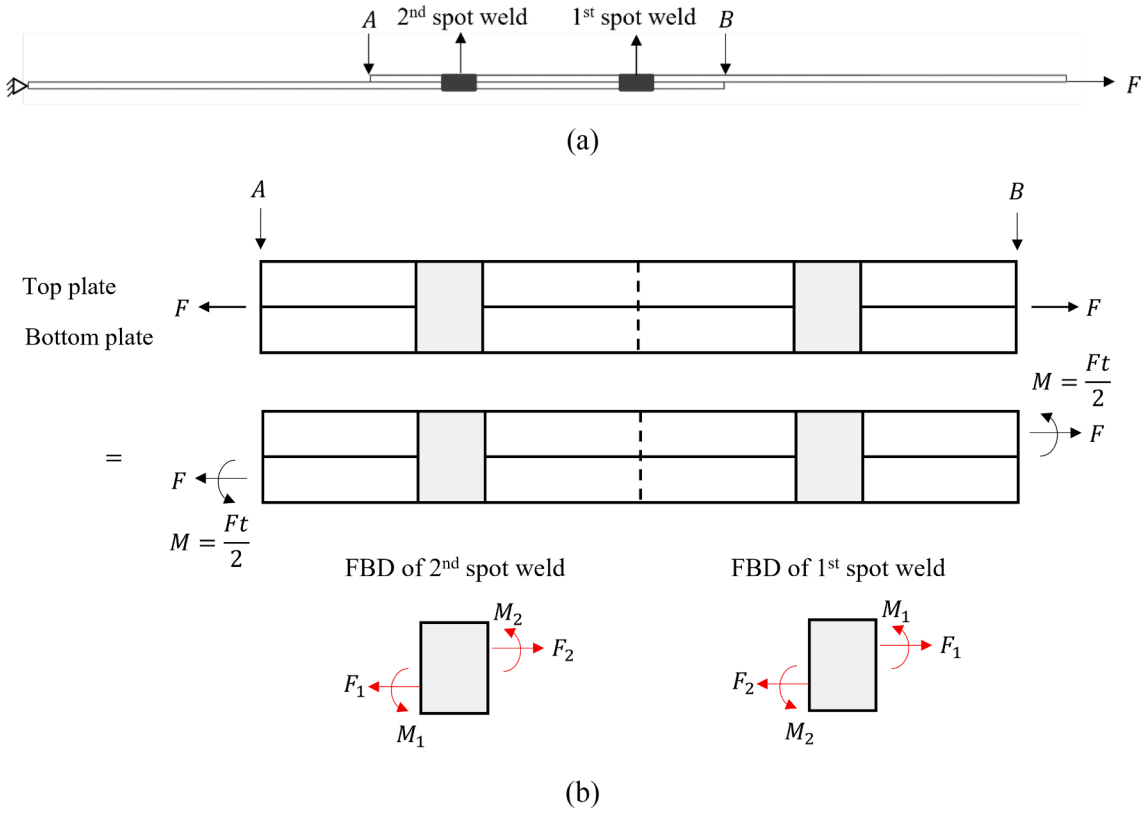

Fig. 17. (a) The side view of the lap-shear specimen with double spot welds in series and (b) the free body diagrams for the top/bottom plates and 1st/2nd spot welds.

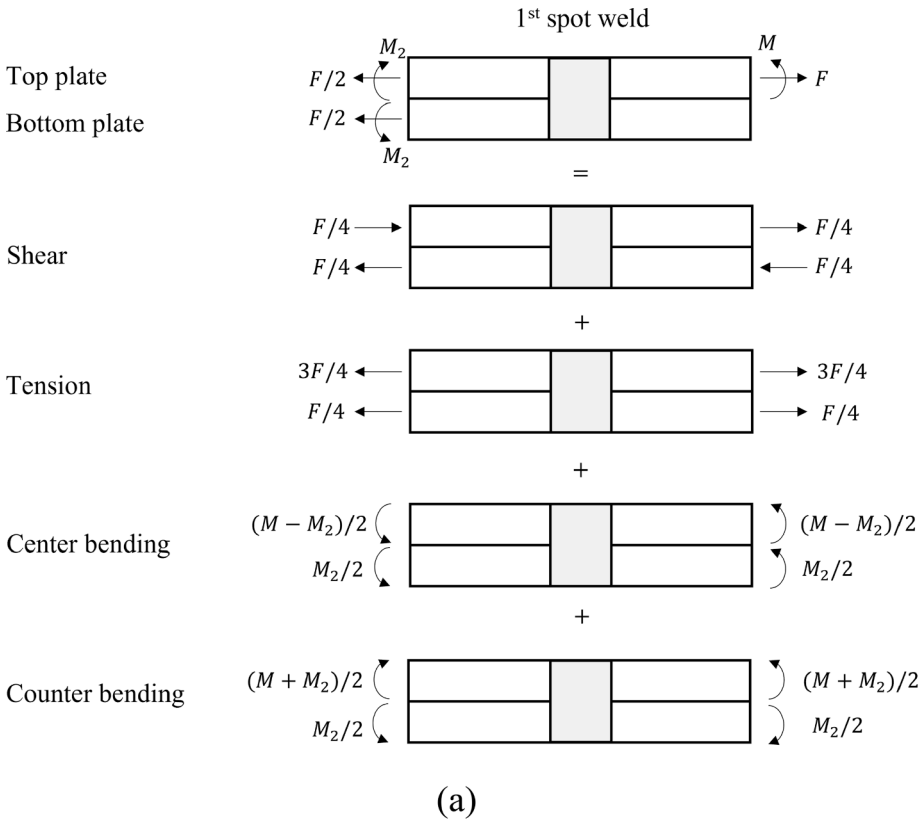

Fig. 18. The schematics of the decomposition process of the shear resultant force for (a) 1st spot weld and (b) 2nd spot weld in a lap-shear specimen with double spot welds in series.

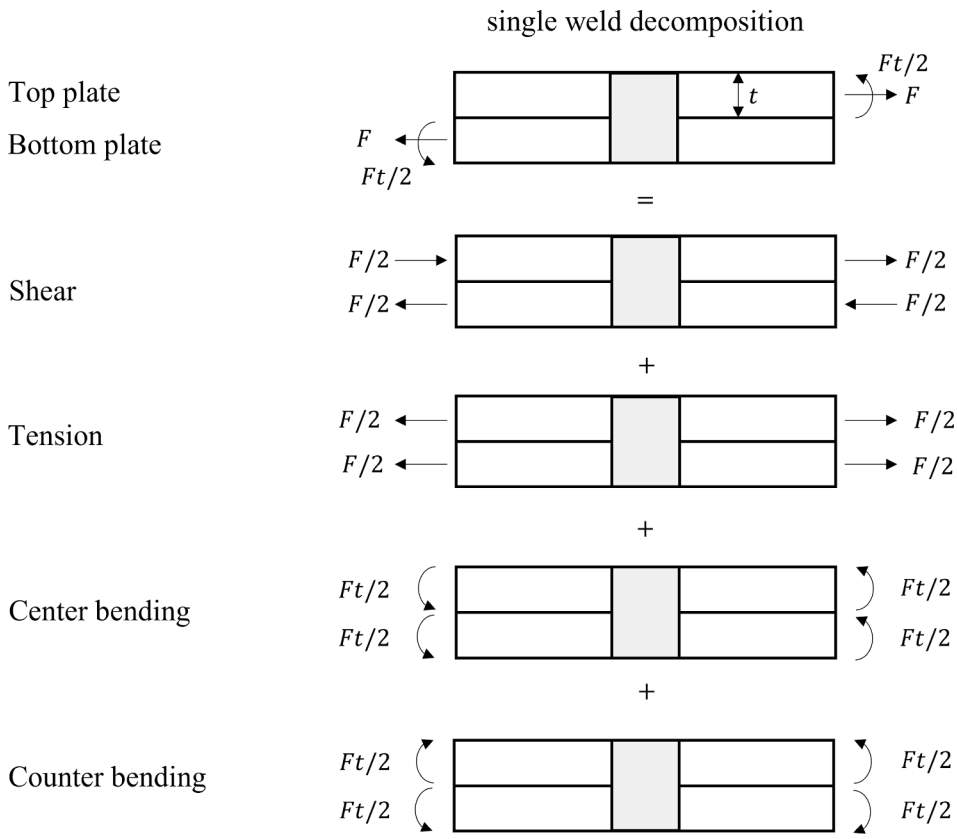

Fig. 19. The schematics of the decomposition process of the shear resultant force for single weld in a lap-shear specimen.

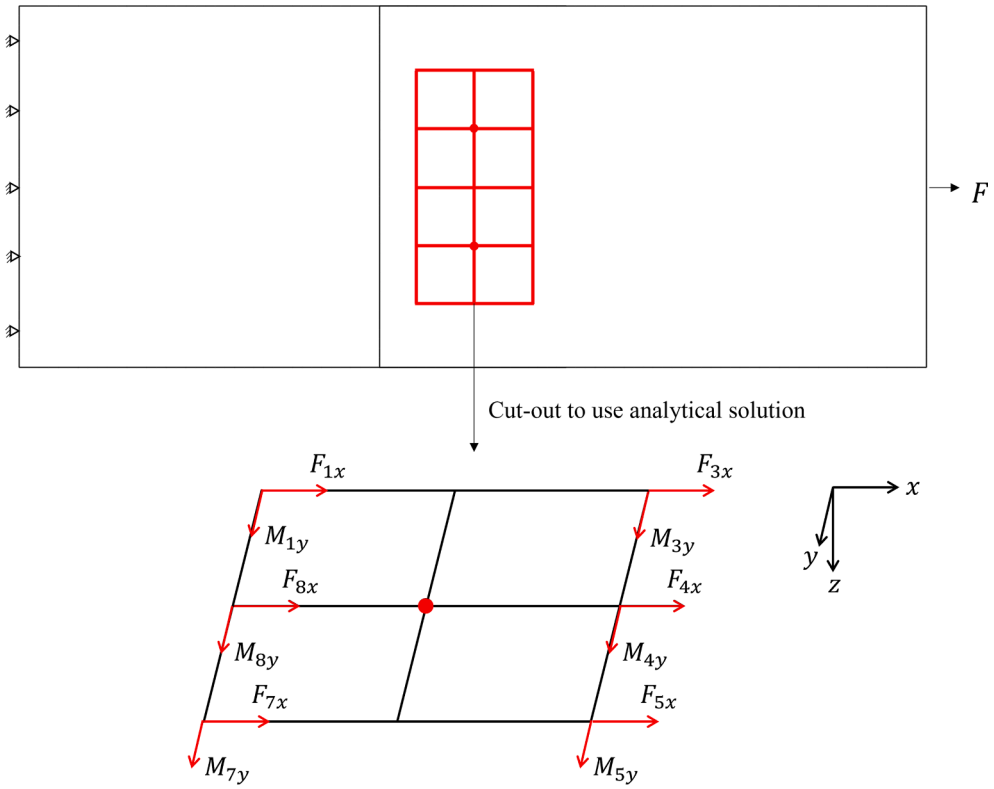

Fig. 20. The top view of a lap-shear specimen with double spot welds in parallel and the cut-out square domain for applying analytical solutions.

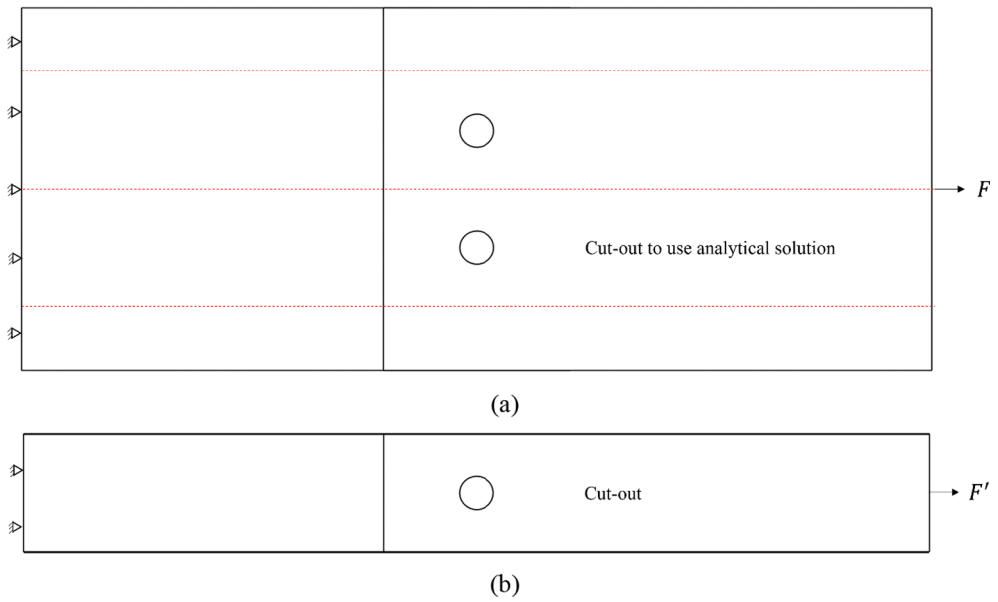

Fig. 21. (a) The top view of a lap-shear specimen with double spot welds in parallel and (b) the cut-out (lap-shear specimen with single spot weld) for applying analytical solutions.

5. Conclusion

A new hybrid structural stress method is presented in this paper for significantly simplifying spot weld representations in fatigue evaluation of complex structures while retaining a high degree of accuracy in structural stress computation. The method is formulated by extracting nodal forces and moments around a group of domain elements connected to a spot weld represented by a regular beam element. Through a systematic decomposition technique, existing closed-form solutions, previously only valid for modeling single spot weld test specimens, can now be used for calculating the relevant structural stresses under simple loading mode conditions. The superposition of the structural stress solutions corresponding to decomposed simple loading modes leads to the actual structural stress solution for each spot weld in a given structure. The accuracy of the hybrid structural stress method proposed is validated by the mesh-insensitive structural stress method (referred to as the direct method in this paper) which requires explicit spot weld representation and is not suitable for applications in complex structures. As a result, the hybrid structural stress method offers the following advantages:

(a) Simple representation of a welded connection in coarse-mesh structural models
(b) Accurate structural stress estimations at critical weld and critical weld nugget edge position
(c) Data transferability for collapsing small lab specimen fatigue test data
(d) Structural life predictability, i.e., using small lab single spot-welded test specimen test data for inferring complex multiple spot-welded components.

Declaration of Competing Interest

The authors declare that they have no known competing financial interests or personal relationships that could have appeared to influence the work reported in this paper.

Acknowledgement

The first two authors (LZ and PD) acknowledge the financial support in part through a Research Incentive fund at the University of Michigan College of Engineering and in part through a National Science Foundation Grant (NSF CMMI 2126163).

Appendix A. Detailed decompositions of nodal Forces/Moments with respect to available analytical stress Solutions.

The decompositions of the nodal forces and nodal moments at the eight nodal points around weld shown in Fig. 4 are presented in this section. Fig. A1a shows a schematic of a decomposition of the in-plane nodal forces into the in-plane edge forces. The left, top, right, and bottom edges of the coarse mesh are named as edge A, B, C, and D, respectively. The 16 in-plane nodal forces are calculated into 4 edge forces by:

$$\begin{aligned} F_{Ax} &= F_{1x} + F_{8x} + F_{7x} + (F_{2x} + F_{6x})/2 \\ F_{Cx} &= F_{3x} + F_{4x} + F_{5x} + (F_{2x} + F_{6x})/2 \\ F_{By} &= F_{1y} + F_{2y} + F_{3y} + (F_{4y} + F_{8y})/2 \\ F_{Dy} &= F_{5y} + F_{6y} + F_{7y} + (F_{4y} + F_{8y})/2 \end{aligned} \tag{A1}$$

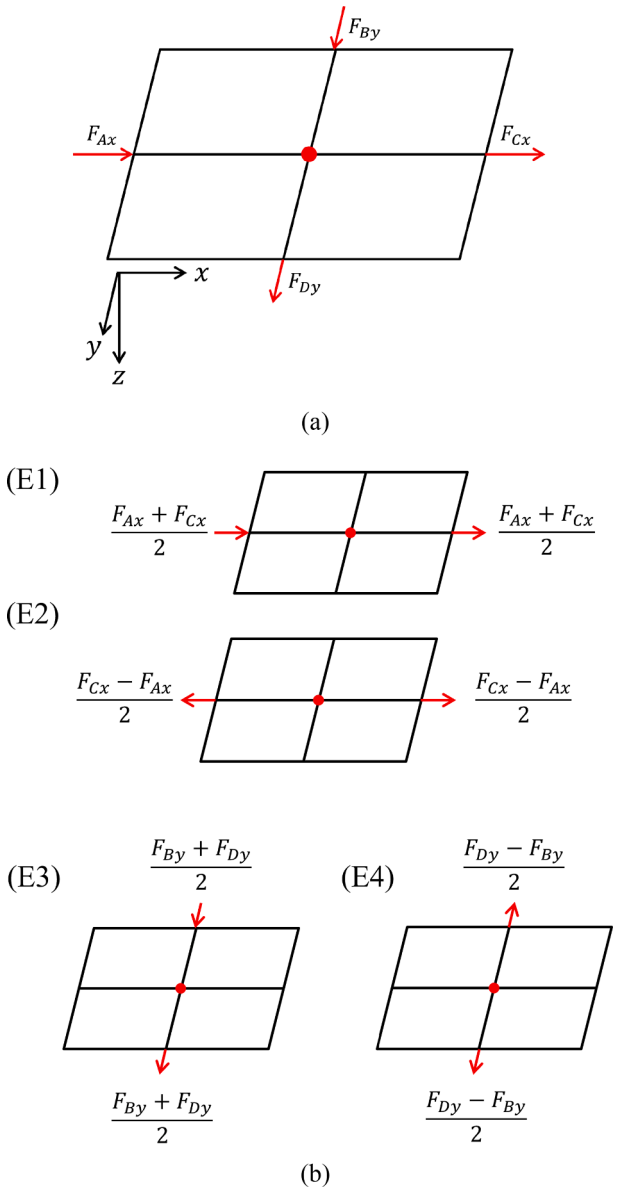

Fig. A1. (a) The in-plane edge forces calculated from the in-plane nodal forces and (b) the decomposition of the in-plane edge forces with respect to available analytical stress solutions.

where F_{Ax},F_{By},F_{Cx}, and F_{Dy} are the edge forces at the left, top, right, and bottom edges of the coarse mesh. Fig. A1b shows a schematic of a decomposition of the in-plane edge forces into four simple loading conditions. The simple loading condition E1 is the in-plane shear force along x direction. The simple loading condition E2 is the in-plane tension force along x direction. The simple loading condition E3 is the in-plane shear force along y direction. The simple loading condition E4 is the in-plane tension force along y direction. The analytical solutions for a plate with a rigid inclusion under in-plane shear and tension forces are presented in Sung and Pan [17].

Fig. A2a shows a schematic of a decomposition of the nodal moments into the edge moments. The 16 nodal moments are calculated to 4 edge moments by:

$$\begin{aligned} M_{Ay} &= M_{1y} + M_{8y} + M_{7y} + (M_{2y} + M_{6y})/2 \\ M_{Cy} &= M_{3y} + M_{4y} + M_{5y} + (M_{2y} + M_{6y})/2 \\ M_{Bx} &= M_{1x} + M_{2x} + M_{3x} + (M_{4x} + M_{8x})/2 \\ M_{Dx} &= M_{5x} + M_{6x} + M_{7x} + (M_{4x} + M_{8x})/2 \end{aligned} \tag{A2}$$

where M_{Ay},M_{Bx},M_{Cy}, and M_{Dx} are the edge moments at the left, top, right, and bottom edges of the coarse mesh. Fig. A2b shows a schematic of a decomposition of the edge moments into four simple loading conditions. The simple loading condition E5 is the center bending moment along y direction. The simple loading condition E6 is the counter bending moment along y direction. The simple loading condition E7 is the center bending moment along x direction. The simple loading condition E8 is the counter bending moment along x direction. The analytical solutions for a plate with a rigid inclusion under the center bending and counter bending moments are presented in Sung and Pan [17].

Fig. A3 to Fig. A6 are the decompositions of the out-of-plane nodal forces. The simple loading conditions E9 and E10 in Fig. A3 are the opening

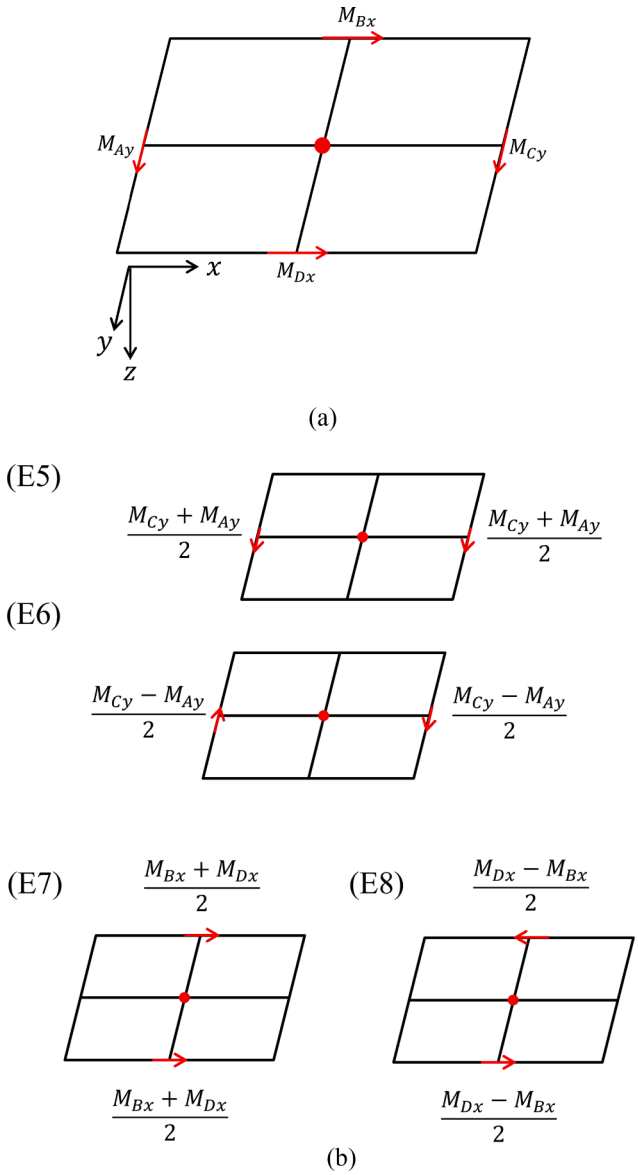

Fig. A2. (a) The edge moments calculated from the nodal moments and (b) the decomposition of the edge moments with respect to available analytical stress solutions.

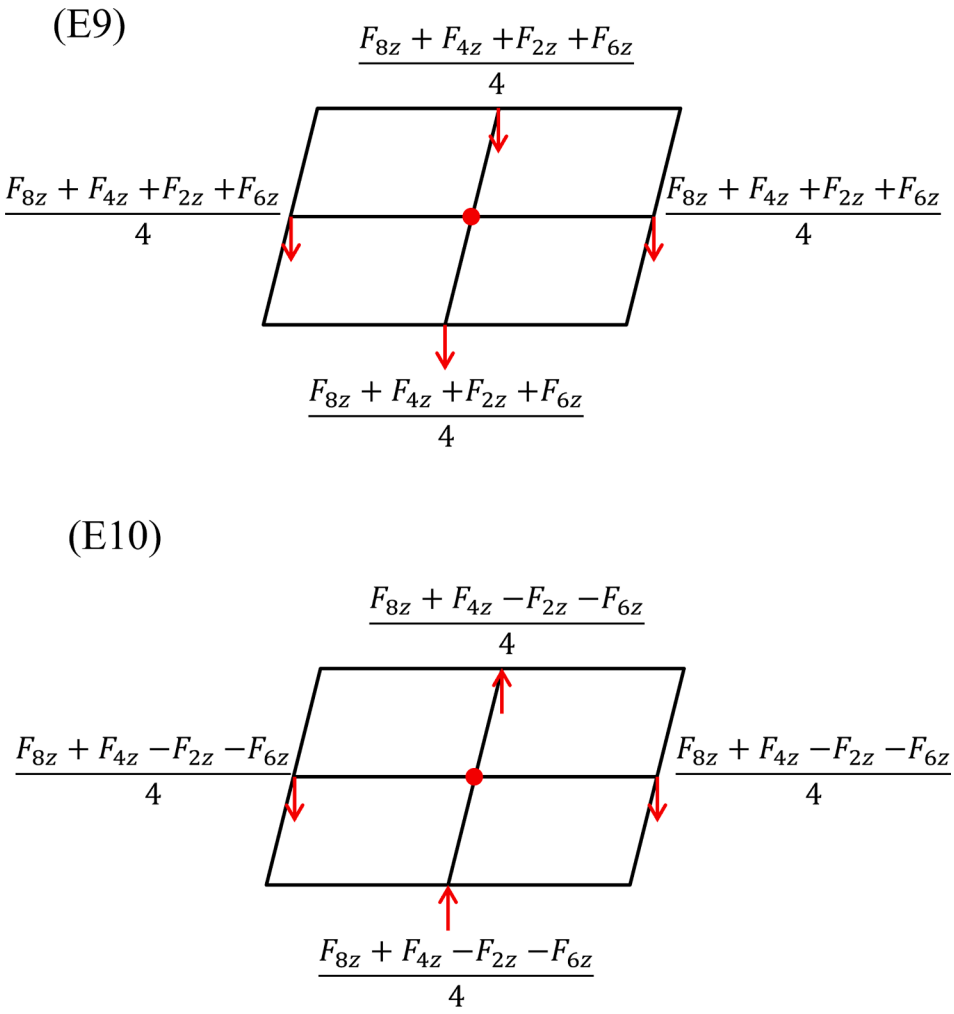

Fig. A3. The decomposition of the out-of-plane nodal forces (E9 and E10) with respect to available analytical stress solutions.

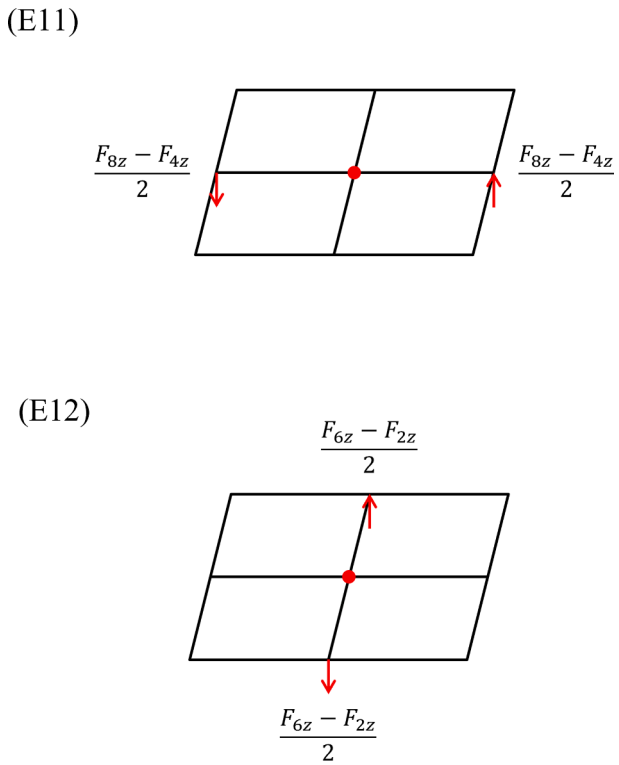

Fig. A4. The decomposition of the out-of-plane nodal forces (E11 and E12) with respect to available analytical stress solutions.

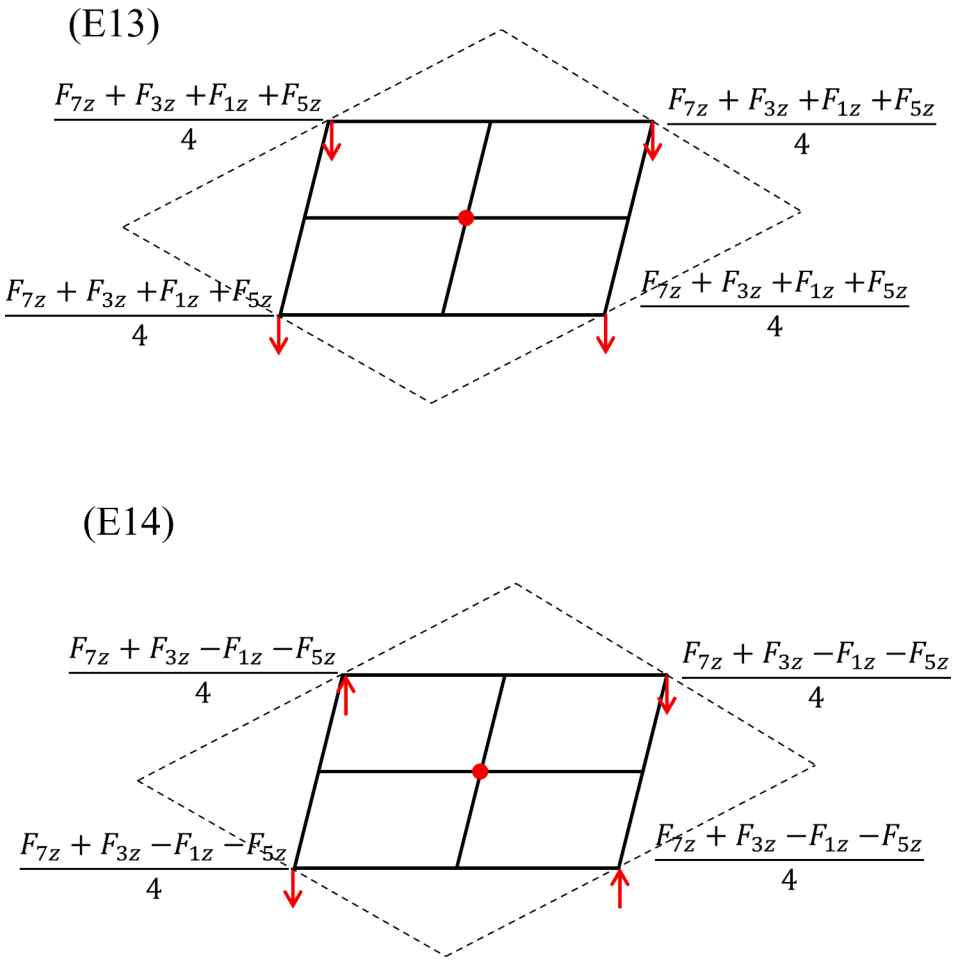

Fig. A5. The decomposition of the out-of-plane nodal forces (E13 and E14) with respect to available analytical stress solutions.

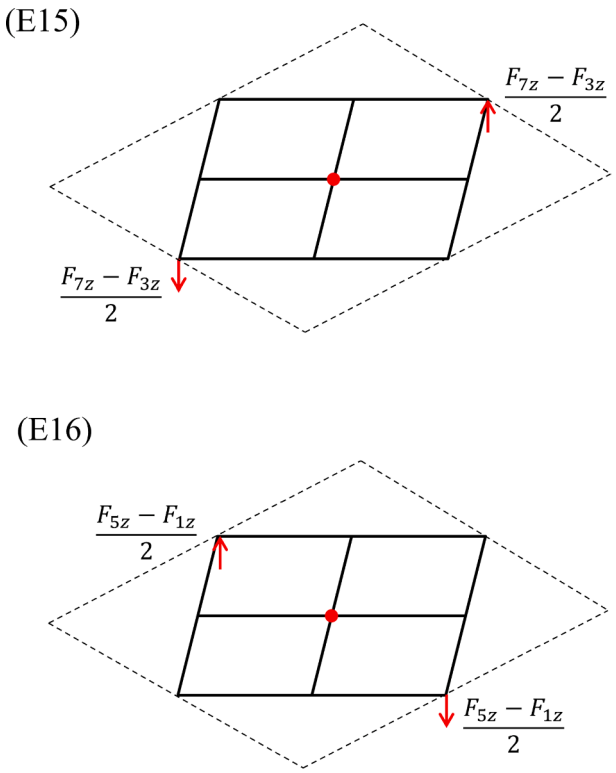

Fig. A6. The decomposition of the out-of-plane nodal forces (E15 and E16) with respect to available analytical stress solutions.

force along z direction and cross counter bending moments, respectively. The simple loading conditions E11 and E12 in Fig. A4 are the center bending moments along y and x directions, respectively. The simple loading conditions E13 and E14 in Fig. A5 are the opening force along z direction and cross counter bending moments for the larger coarse mesh (black dashed mesh) which is similar to that in Fig. A3 but with a counter clock-wise rotation about z axis of $\frac{\pi}{4}$ and a larger edge length of $\sqrt{2}b$. Similarly, the simple loading conditions E15 and E16 are the center bending moments for the larger coarse mesh (black dashed mesh). The analytical solutions for the opening force and cross counter bending moments are presented in Lin and Pan [9,16].and Sung and Pan [17].

Appendix B. Coarse-Mesh hybrid structural stress method on Lap-Shear and Coach-Peel specimens with single spot weld

Fig. B1a and b show FE models of the lap-shear and coach-peel specimens for the direct structural stress method, respectively. In the FE models, one side of the specimen marked in red was constrained in all directions and the other side of the specimen marked in blue was constrained in all directions except the direction of the loading that was applied at the center of the grip region. The loads are applied at reference points located at the center of the grip region and the other elements in the corresponding grip regions are connected to the reference points by rigid body constraints in Abaqus. The Abaqus linear shell element S4 is exclusively used throughout the models.

Fig. B2a and b show FE models of the lap-shear and coach-peel specimens for the coarse-mesh hybrid structural stress method with mesh size b of 9.5 mm, respectively. The boundary conditions are the same as those for the direct structural stress method as shown in Fig. B1. As shown in Fig. B2, the welds are represented by beam elements. The pre-defined square-shaped domain is marked as a red square. Mesh-insensitivity study is also conducted in the lap-shear and coach-peel specimens with single spot weld. Three mesh sizes with b/a of 2.72, 3.39, and 4.07 are used for the mesh-insensitivity study.

Since the structural stress analytical solutions for the lap-shear and coach-peel specimens with single spot weld are available in the literature [9,16,17], both the structural stresses obtained using the direct structural stress method and coarse-mesh hybrid structural stress method are compared with the analytical solutions. Fig. B3a shows the radial structural stress σ_{rr} distribution around weld nugget edge in the lap-shear specimen with different mesh sizes based on the analytical solution presented in Sung and Pan [17]. The results obtained from the direct structural stress method and coarse-mesh hybrid structural stress method have similar radial structural stress σ_{rr} distributions. However, the maximum radial structural stress $\sigma_{rr_{max}}$ obtained from the coarse-mesh hybrid structural stress method is slightly lower than that obtained from the direct structural stress method. The maximum radial structural stress $\sigma_{rr_{max}}$ obtained from the analytical solution is close to that obtained from the direct structural stress method as shown in Fig. B3a.

Fig. B3b shows the radial structural stress σ_{rr} distribution around weld nugget edge in the coach-peel specimens with different mesh sizes based on

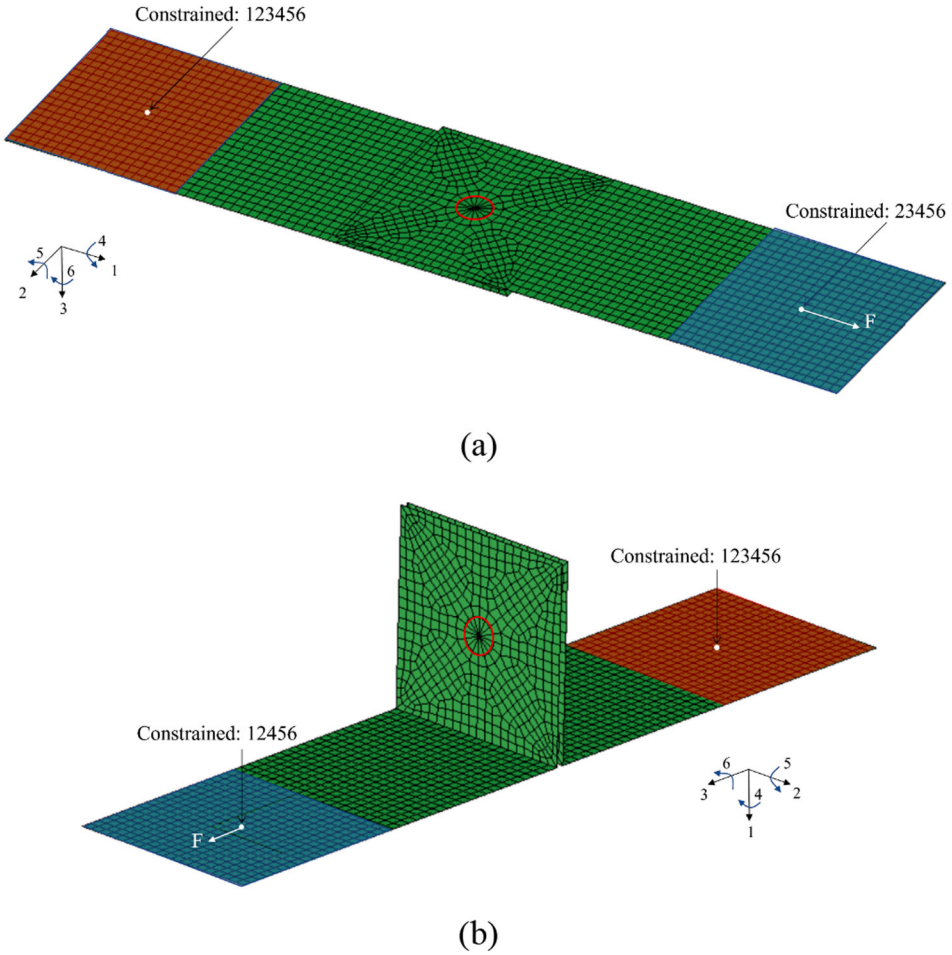

Fig. B1. The FE models for direct structural stress method for the (a) lap-shear specimen and (b) coach-peel specimen.

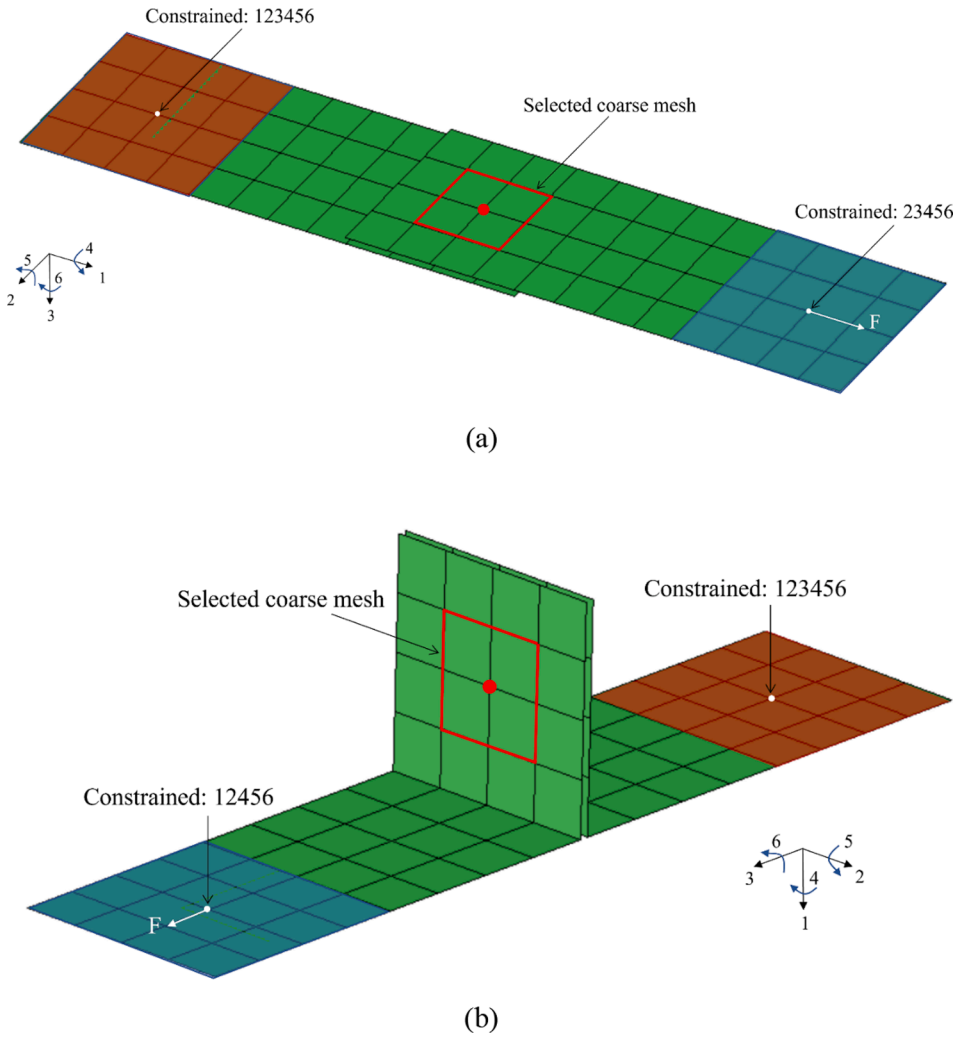

Fig. B2. The FE models for hybrid structural stress method for the (a) lap-shear specimen and (b) coach-peel specimen.

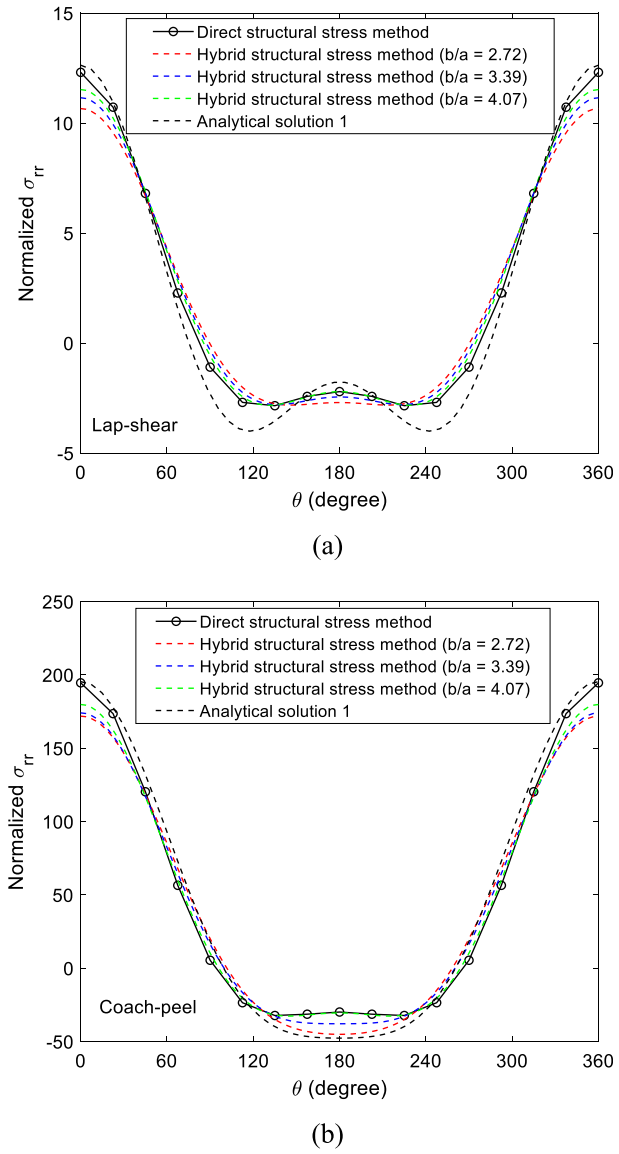

Fig. B3. The computational radial structural stress distributions around weld nugget edge of the (a) lap-shear and (b) coach-peel specimens with single spot weld.

the analytical solution presented in Sung and Pan [17]. Similarly, the radial structural stress σ_{rr} distributions obtained from the direct method and coarse-mesh hybrid structural stress method agree with each other. But the maximum radial structural stress $\sigma_{rr_{\max}}$ obtained from the coarse-mesh hybrid structural stress method is slightly lower than that from the direct method. Instead, the maximum radial structural stress $\sigma_{rr_{\max}}$ obtained from the analytical solution is close to that obtained from the direct method as shown in Fig. B3b.

Small mesh size effect is observed in Fig. B3a and b that smaller b/a ratio results lower maximum radial structural stress $\sigma_{rr_{\max}}$. The reasons for the small mesh size effect of the coarse-mesh hybrid structural stress method are discussed in Section 4.

References

[1] Bhatti QI, Ouisse M, Cogan S. An adaptive optimization procedure for spot-welded structures. Comput Struct 2011;89(17-18):1697–711.

[2] Junqueira DM, Silveira ME, Ancelotti AC. Analysis of spot weld distribution in a weldment—numerical simulation and topology optimization. Int J Adv Manuf Technol 2018;95(9-12):4071–9.

[3] Yan L, Guo Q-T, Yang S, Liao X-W, Qi C. A size optimization procedure for irregularly spaced spot weld design of automotive structures. Thin-Walled Struct 2021;166:108015. https://doi.org/10.1016/j.tws.2021.108015.

[4] Dong P. Quantitative weld quality acceptance criteria: an enabler for structural lightweighting and additive manufacturing. Welding J 2020;99(2):39s–51s.

[5] Zhang J, Dong P. A hybrid polygonal element method for fracture mechanics analysis of resistance spot welds containing porosity. Eng Fract Mech 1998;59(6):815–25.

[6] Rupp A, Störzel K, Grubisic V. Computer aided dimensioning of spot-welded automotive structures. SAE Technical Paper 1995.

[7] Radaj D, Zhang S. Stress intensity factors for spot welds between plates of unequal thickness. Eng Fract Mech 1991;39(2):391–413.

[8] Gao Y, Chucas D, Lewis C, McGregor IJ. Review of CAE fatigue analysis techniques for spot-welded high strength steel automotive structures. SAE Trans 2001,:738–50.

[9] Lin P-C, Pan J. Closed-form structural stress and stress intensity factor solutions for spot welds in commonly used specimens. Eng Fract Mech 2008;75(18):5187–206.

[10] Wei C, Kang HT. Fatigue life prediction of spot-welded joints with a notch stress approach. Theor Appl Fract Mech 2020;106:102491. https://doi.org/10.1016/j.tafmec.2020.102491.

[11] Qin Y, Xiao S, Lu L, Yang B, Li X, Yang G. Structural stress–fatigue life curve improvement of spot welding based on quasi-newton method. Chin J Mech Eng 2020;33(1):1–12.
[12] Salvini P, Scardecchia E, Vivio F. Fatigue life prediction on complex spot welded joints. SAE Trans 1997,:967–75.
[13] Dong P. A structural stress definition and numerical implementation for fatigue analysis of welded joints. Int J Fatigue 2001;23(10):865–76.
[14] Dong P. A robust structural stress procedure for characterizing fatigue behavior of welded joints. SAE Trans 2001,:89–100.
[15] Kang H, Dong P, Hong J. Fatigue analysis of spot welds using a mesh-insensitive structural stress approach. Int J Fatigue 2007;29(8):1546–53.
[16] Lin P-C, Pan J. Closed-form structural stress and stress intensity factor solutions for spot welds under various types of loading conditions. Int J Solids Struct 2008;45 (14-15):3996–4020.
[17] Sung S-J, Pan J. Accurate analytical structural stress and stress intensity factor solutions for similar and dissimilar spot welds in lap-shear specimens. Eng Fract Mech 2017;182:265–86.
[18] Zhang S. Stress intensities at spot welds. Int J Fract 1997;88(2):167–85.
[19] Zhang J, Dong P, Gao Y. Evaluation of stress intensity factor-based predictive technique for fatigue life of resistance spot welds. SAE Trans 2001,:704–13.
[20] Salvini P, Vivio F, Vullo V. A spot weld finite element for structural modelling. Int J Fatigue 2000;22(8):645–56.
[21] Yang L, Yang B, Yang G, Xiao S, Zhu T, Wang F. A comparative study of fatigue estimation methods for single-spot and multispot welds. Fatigue Fract Eng Mater Struct 2020;43(6):1142–58.
[22] Dong P, Hong JK, Osage DA, Dewees DJ and Prager M. The master SN curve method an implementation for fatigue evaluation of welded components in the ASME B&PV Code, Section VIII, Division 2 and API 579-1/ASME FFS-1. Welding Research Council Bulletin, (523). 2010.
[23] Dong P, Hong JK. CAE weld durability prediction: a robust single damage parameter approach. SAE Tech Paper 2002.
[24] Dong P, Wei Z, Hong JK. A path-dependent cycle counting method for variable-amplitude multi-axial loading. Int J Fatigue 2010;32(4):720–34.
[25] Wei Z, Dong P. Multiaxial fatigue life assessment of welded structures. Eng Fract Mech 2010;77(15):3011–21.
[26] Mei J, Dong P. A new path-dependent fatigue damage model for non-proportional multi-axial loading. Int J Fatigue 2016;90:210–21.
[27] Dong P, Pei X, Xing S, Kim MH. A structural strain method for low-cycle fatigue evaluation of welded components. Int J Press Vessels Pip 2014;119:39–51.
[28] Pei X, Dong P, Xing S. A structural strain parameter for a unified treatment of fatigue behaviors of welded components. Int J Fatigue 2019;124:444–60.
[29] Pei X, Dong P. An analytically formulated structural strain method for fatigue evaluation of welded components incorporating nonlinear hardening effects. Fatigue Fract Eng Mater Struct 2019;42(1):239–55.
[30] Abaqus version 6.14 User's Manual.
[31] Zhang L, Sung S-J, Pan J, Su X, Friedman P. Closed-form structural stress solutions for fatigue life estimations of flow drill screw joints in lap-shear specimens of aluminum 6082–T6 sheets. SAE Int J Mater Manuf 2017;10(2):154–9.
[32] Mei J, Dong P, Xing S, Vasu A, Ganamet A, Chung J. An overview and comparative assessment of approaches to multi-axial fatigue of welded components in codes and standards. Int J Fatigue 2021;146:106144.
[33] Ravi SK, Dong P, Wei Z. Data-driven modeling of multiaxial fatigue in frequency domain. Marine Structures 2022;84:103201.
[34] Pei X, Ravi SK, Dong P, Li X, Zhou X. A multi-axial vibration fatigue evaluation procedure for welded structures in frequency domain. Mechanical Systems and Signal Processing 2022;167:108516.
[35] Pei X, Li X, Zhao S, Dong P, Liu X, Xie M. Low cycle fatigue evaluation of welded structures with arbitrary stress-strain curve considering stress triaxiality effect. Int J Fatigue 2022;162:106969.